Estuaries and Coasts (2024) 47:2283–2305
https://doi.org/10.1007/s12237-024-01421-z

Influence of Rivers, Tides, and Tidal Wetlands on Estuarine Carbonate System Dynamics

Fei Da[1,2] · Marjorie A. M. Friedrichs[2] · Pierre St-Laurent[2] · Raymond G. Najjar[3] · Elizabeth H. Shadwick[4] · Edward G. Stets[5]

Received: 26 February 2024 / Revised: 11 June 2024 / Accepted: 12 August 2024 / Published online: 18 September 2024

Abstract

Variations in estuarine carbonate chemistry can have critical impacts on marine calcifying organisms, yet the drivers of this variability are difficult to quantify from observations alone, due to the strong spatiotemporal variability of these systems. Terrestrial runoff and wetland processes vary year to year based on local precipitation, and estuarine processes are often strongly modulated by tides. In this study, a 3D-coupled hydrodynamic-biogeochemical model is used to quantify the controls on the carbonate system of a coastal plain estuary, specifically the York River estuary. Experiments were conducted both with and without tidal wetlands. Results show that on average, wetlands account for 20–30% of total alkalinity (TA) and dissolved inorganic carbon (DIC) fluxes into the estuary, and double-estuarine CO_2 outgassing. Strong quasi-monthly variability is driven by the tides and causes fluctuations between net heterotrophy and net autotrophy. On longer time scales, model results show that in wetter years, lower light availability decreases primary production relative to biological respiration (i.e., greater net heterotrophy) resulting in substantial increases in CO_2 outgassing. Additionally, in wetter years, advective exports of DIC and TA to the Chesapeake Bay increase by a factor of three to four, resulting in lower concentrations of DIC and TA within the estuary. Quantifying the impacts of these complex drivers is not only essential for a better understanding of coastal carbon and alkalinity cycling, but also leads to an improved assessment of the health and functioning of coastal ecosystems both in the present day and under future climate change.

Keywords Chesapeake Bay · Carbonate system (CO_2 system) · Rivers · Tidal wetlands · Tides

Communicated by Dennis Swaney

Highlights
- A numerical model was used to study estuarine carbonate chemistry variability.
- DIC and TA fluxes from tidal wetlands double estuarine CO_2 outgassing.
- Tides drive quasi-monthly variability between net heterotrophy and autotrophy.
- Rivers drive strong year-to-year variability in DIC and TA fluxes and concentrations.
- In wetter years, DIC and TA export from the estuary increases by 3 to 4 times.

✉ Fei Da
fd6996@princeton.edu; feida6996@gmail.com

Marjorie A. M. Friedrichs
marjy@vims.edu

[1] Department of Geoscience, Princeton University, Princeton, NJ, USA

[2] Virginia Institute of Marine Science, William & Mary, Gloucester Point, VA, USA

[3] Department of Meteorology and Atmospheric Science, The Pennsylvania State University, University Park, PA, USA

[4] Commonwealth Scientific and Industrial Research Organisation (CSIRO), Environment, Hobart, TAS, Australia

[5] United States Geological Survey, Mounds View, MN, USA

Introduction

Positioned at the land–ocean interface, the coastal zone plays a crucial role in the global carbon cycle and the delivery of vital ecosystem services, despite its relatively small area on the Earth's surface. Here, many physical and biogeochemical processes modulate and transform carbon inputs from terrestrial, intertidal, and oceanic sources, influencing air-sea CO_2 fluxes and carbon flows across the land-to-ocean continuum (Chen and Borges 2009; Cai et al. 2011, 2020; Najjar et al.

2018; Lacroix et al. 2021; Regnier et al. 2022). Understanding the complexity of the carbon cycle in coastal zones is important for shaping effective global carbon and climate policies (Dai et al. 2022). Moreover, coastal water bodies, including estuaries, serve as critical habitats for economically, culturally, and ecologically important marine species. Given the prevailing negative impacts of high partial pressure of CO_2 (pCO_2) on coastal invertebrates (Vargas et al. 2022), it is particularly crucial to understand the multiple processes that collectively impact the coastal carbonate system. Such an improved understanding of changing carbonate chemistry will also provide insights into both present day and potential future changes in ecosystem services provided by the coastal zone, including fisheries and shellfish aquaculture (Ekstrom et al. 2015; Doney et al. 2020).

The coastal carbonate system is profoundly influenced by terrestrial, intertidal, and oceanic processes. In general, these processes simultaneously impact mixing, biological activities (e.g., primary production and respiration), and air-sea CO_2 exchange, which are the key mechanisms impacting the concentrations of dissolved inorganic carbon (DIC) and total alkalinity (TA) in estuarine ecosystems (Wang and Cai 2024). Given the proximity of estuaries to land, terrestrial inputs strongly impact the spatial and temporal gradients of carbonate chemistry via riverine delivery of freshwater (Salisbury et al. 2008; Hu et al. 2020), carbon and alkalinity (Raymond and Oh 2009; Kaushal et al 2013; Stets et al. 2014; Raymond and Hamilton 2018; Savoie et al. 2022), and nutrients (Feely et al. 2010; Cai et al. 2011, 2020; Wallace et al. 2014; Van Dam and Wang 2019). Additionally, although intertidal zones such as tidal wetlands are spatially limited, their highly productive coastal vegetation provides a large source of DIC and TA to estuarine waters via lateral advection (Odum 1980; Wang et al. 2016; Chu et al. 2018; Yao et al. 2022; Yau et al. 2022). As a result, tidal wetlands play a crucial role in the estuarine carbonate system and regional carbon and alkalinity budgets (Hu and Cai et al. 2011; Najjar et al. 2018; Alongi 2020; Santos et al. 2021; Reithmaier et al. 2023). Finally, estuarine waters are directly influenced by oceanic forces via tidal cycles and gravitational circulation, which further impact physical and biogeochemical controls on the estuarine carbonate system (Sims et al. 2022; Scully et al. 2022).

The York River Estuary (YRE), a tributary of the Chesapeake Bay (Fig. 1), is an example of an estuary that has extensive tidal wetlands (Mitchell et al. 2017), making it ideal for studying the impacts of tidal wetlands on estuarine biogeochemistry. In the YRE, the ratio of tidal wetland area (78 km^2; Mitchell et al. 2017) to estuarine surface area (194 km^2) is 0.40, which is much higher than the average ratio for eastern North America (0.27; Najjar et al. 2018) and the globe (0.17–0.28; Regnier et al. 2022). The YRE consists

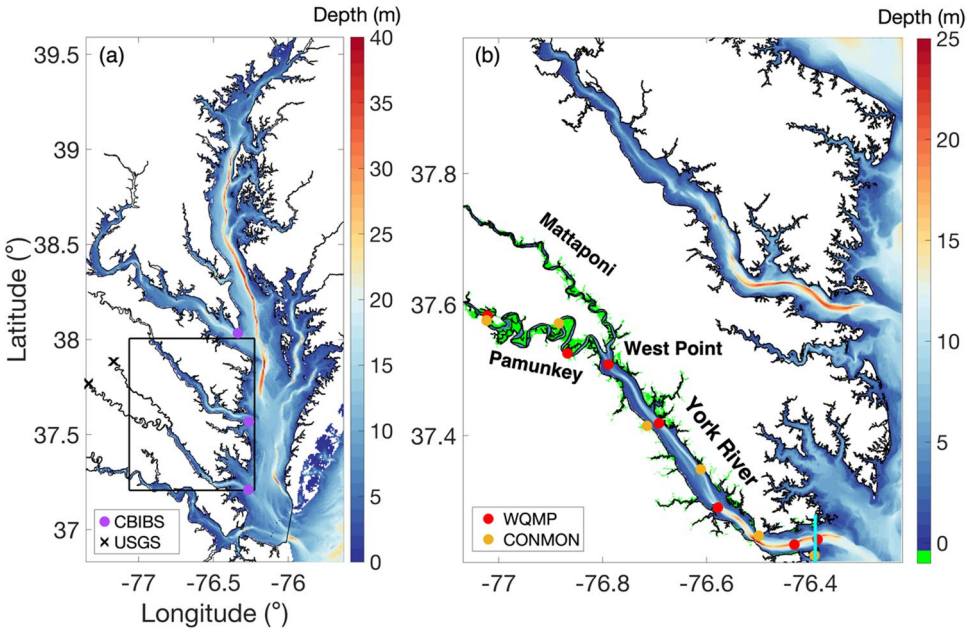

Fig. 1 The horizontal grid and bathymetry of **a** the Chesapeake Bay model and **b** the YRE model. Black rectangle in **a** outlines the YRE model domain in **b**. Green areas in **b** represent tidal wetlands. Red and yellow circles denote stations with WQMP data and CONMON data used for model evaluation (Table 1). From north to south, the WQMP stations are TF4.2, RET4.1, RET4.3, LE4.1, LE4.2, LE4.3, and WE4.2 and the CONMON stations are White House Landing, Sweet Hall Marsh, Taskinas Creek, Claybank, Gloucester Point, and Goodwin Island. Purple circles in **a** denote CBIBS stations. Black x's in **a** represent the USGS gauge stations where historical TA data are available (station ID numbers 01673000 and 01674500). The cyan line in **b** represents the mouth of the YRE as defined in this study

of two main tributaries (the Pamunkey and Mattaponi Rivers) as well as the main York River, which extends from the Goodwin Islands to West Point where the two tributaries merge (Fig. 1). Downstream of West Point, the YRE has an average water depth of 4.9 m (Cronin 1971) and average width of 3.8 km (Nichols et al. 1991), whereas its two main tributaries are much shallower and narrower. As the fifth largest sub-estuary of the Chesapeake Bay (Reay 2009), the YRE receives freshwater discharge at a mean rate of 65 m^3 s^{-1} (averaged over the years 1985–2020). In 2018, the Chesapeake Bay watershed experienced the wettest year in over 124 years of recordkeeping (National Centers for Environmental Information 2019), and the annual mean river inflow to the YRE reached 92 m^3 s^{-1}. In a partially mixed estuary like the YRE, stronger river inflow enhances estuarine circulation and decreases residence time (Shen and Haas 2004). Although the YRE is classified as a microtidal estuary, tides play a crucial role in mixing and sediment dynamics (Haas 1977; Scully and Friedrichs 2007a,b; Friedrichs 2009). In most estuaries, the largest two tidal constituents are M_2 and S_2, which represent the largest lunar and solar constituent directly related to the gravitational effect of the Moon and Sun on the tides. In the YRE, however, M_2 is followed by N_2 as the second largest constituent, representing the effect of the non-circularity of the Moon's orbit (see the harmonics at station 8637689; NOAA Tides and Currents n.d.). The interactions between M_2 and N_2 result in a quasi-monthly tidal cycle (27.5 days) in addition to the spring-neap cycle (Byun and Hart 2020). These regular oscillations have the potential to substantially modify turbulent mixing and stratification and in turn biogeochemical activity.

While water quality issues related to eutrophication, harmful algal blooms, and hypoxia have been well studied in the YRE (Lake and Brush 2015; Reece 2015; Mulholland et al. 2018; Qin and Shen 2019; Kim et al. 2021), there has been relatively little investigation of carbonate chemistry. Early observations by Raymond et al. (2000) suggested that the YRE is a source of atmospheric CO_2 due to net heterotrophy, whereas net sulfate reduction in estuarine and tidal wetland sediments most likely sustains TA above expectations based on conservative mixing assumptions. Recent data analyses support these findings of CO_2 outgassing in the Pamunkey and Mattaponi (Bukaveckas 2022) and TA production (Najjar et al. 2020). Using high-frequency pH measurements in the lower YRE, Shadwick et al. (2019) concluded that circulation (i.e., advection and mixing), biology, and temperature dominate seasonal transitions in the carbonate system. Although these previous observational studies form a basic understanding of the YRE carbonate system, and estuarine biogeochemical modeling studies that include tidal wetlands are starting to emerge (Clark et al. 2020; Cai et al. 2023), it still remains poorly understood as to how terrestrial, intertidal and oceanic drivers collectively impact DIC and TA balances in coastal plain estuaries such as the YRE.

To address this knowledge gap, this study uses a three-dimensional (3D) coupled hydrodynamic-biogeochemical model forced with empirical inputs from tidal wetlands. This modeling system is used to calculate DIC and TA budgets and to investigate how river inputs, tidal wetlands, and tidal modulations impact the YRE carbonate system. This paper first introduces the in situ observations and the 3D estuarine biogeochemistry model used for analyses. Primary results include the annual mean DIC and TA balances, as well as temporal and spatial variability of DIC and TA sources and sinks during the average river flow conditions of 2017 and high river flow conditions of 2018. The "Discussion" section focuses on examining drivers of estuarine ecosystem metabolism, air-sea CO_2 exchange, sources and sinks of TA, and exchanges of DIC and TA between the YRE and the main stem of the Chesapeake Bay.

Method

In Situ Observations in the YRE

A plethora of historical water quality cruise data and high-frequency sensor data are available in the YRE during our study years (2017–2018). Physical and biogeochemical variables have been monitored by the Chesapeake Bay Water Quality Monitoring Program (WQMP) since 1984 (Olson et al. 2012; CBP 2022). This study uses WQMP water temperature, salinity, dissolved oxygen (O_2), and potentiometric pH data at seven stations (Fig. 1) throughout the YRE in 2017 and 2018. These variables at station WE4.2 were measured once each month from September to May, and twice each month from June to August in both years. At the other six stations, data were collected once each month except in April, May, July and December in 2017 and once each month from February to October in 2018. Additionally, high-frequency (15-min interval) water temperature, salinity, O_2, and potentiometric pH data are available at six fixed Continuous Monitoring (CONMON; CBNERR-VA VIMS 2022) stations in the YRE over the years 2017–2018 (Fig. 1). These stations are located near the shoreline (water depth 1 to 3 m) and are shallower than the WQMP stations (water depths 3 to 20 m). The potentiometric pH measurements from both datasets are reported on the NBS scale and have a precision of ± 0.2 pH units or better. Hourly resolution pH data (Shadwick et al. 2019) collected by a SeapHOx sensor in 2017 and 2018 and reported on the total scale with an accuracy of ± 0.02 are available at the National Oceanic and Atmospheric Administration Chesapeake Bay Interpretive Buoy System (CBIBS) York River buoy (Fig. 1). Hourly averaged salinity data in 2017 and 2018 are available

from the CBIBS York River, Stingray Point, and Potomac buoys (Fig. 1). These buoy data are only used to improve open boundary conditions along the edges of the 3D model domain, while WQMP and CONMON data are used for model skill assessment ("Estuarine Carbon Biogeochemistry Model"). Total scale pH data from the SeapHOx sensor are converted to the NBS scale to ensure consistency with other datasets and 3D model results.

Since TA and DIC observations are unavailable for comparison with results from the 3D estuarine model (see "Estuarine Carbon Biogeochemistry Model"), these carbonate system variables are derived from observed temperature, salinity, and pH. Specifically, TA products at the WQMP and CONMON stations are calculated from in situ salinity data and a linear alkalinity to salinity (TA:S) relationship derived from historical YRE data ($TA = 66.7 \times S + 444.5$, $R^2 = 0.95$; Najjar et al. 2020). DIC is then computed from the estimated TA and in situ pH, temperature, and salinity data using CO2SYS (van Heuven et al. 2011) assuming the equilibrium constants of Cai and Wang (1998) as they are suitable for both fresh and estuarine waters (Dinauer and Mucci 2017; Herrmann et al. 2020). These derived TA and DIC products are only used as a secondary metric for model skill assessment and consistency (see "Estuarine Carbon Biogeochemistry Model"). It is important to note that these estimates are inherently associated with errors, particularly stemming from the use of potentiometric pH data.

Historical riverine TA data from 1979 to 1999 are available at two gauging stations operated by the United States Geological Survey (USGS) in the Pamunkey and Mattaponi tributaries of the YRE (Fig. 1). Riverine DIC concentrations at these locations were calculated from temperature, TA, and pH data using the freshwater constants of Plummer and Busenberg (1982) within the geochemical modeling program PHREEQC (Parkhurst and Appelo 1999). Daily estimates of TA and DIC concentration and flux were then developed using the Weighted Regressions on Time Discharge and Seasons (WRTDS) model implemented using the R package EGRET (Hirsch et al. 2010; Hirsch and De Cicco 2015). WRTDS uses daily streamflow values paired with periodic constituent concentration data to develop statistically based estimates of daily concentration and flux from flow condition, season, and accounting for any long-term trends in the observational data. This study uses daily WRTDS TA concentrations and daily USGS discharge data from 1985 to 1993 to develop linear relationships between $\log_{10}$ (discharge) and $\log_{10}$ (river TA), as shown in Fig. 2b, c and Table S2. These relationships capture the flow effect on river TA concentrations and are assumed to hold true in recent years since Najjar et al. (2020) showed no significant trends in TA concentrations in the Pamunkey and Mattaponi Rivers over the past several decades. Ultimately, these relationships are used to create the river TA and DIC forcing of the 3D model (see "Model Forcing").

Estuarine Carbon Biogeochemistry Model

A 3D estuarine-carbon-biogeochemistry model (ECB; Feng et al. 2015; St-Laurent et al. 2020; Da et al. 2021) coupled to

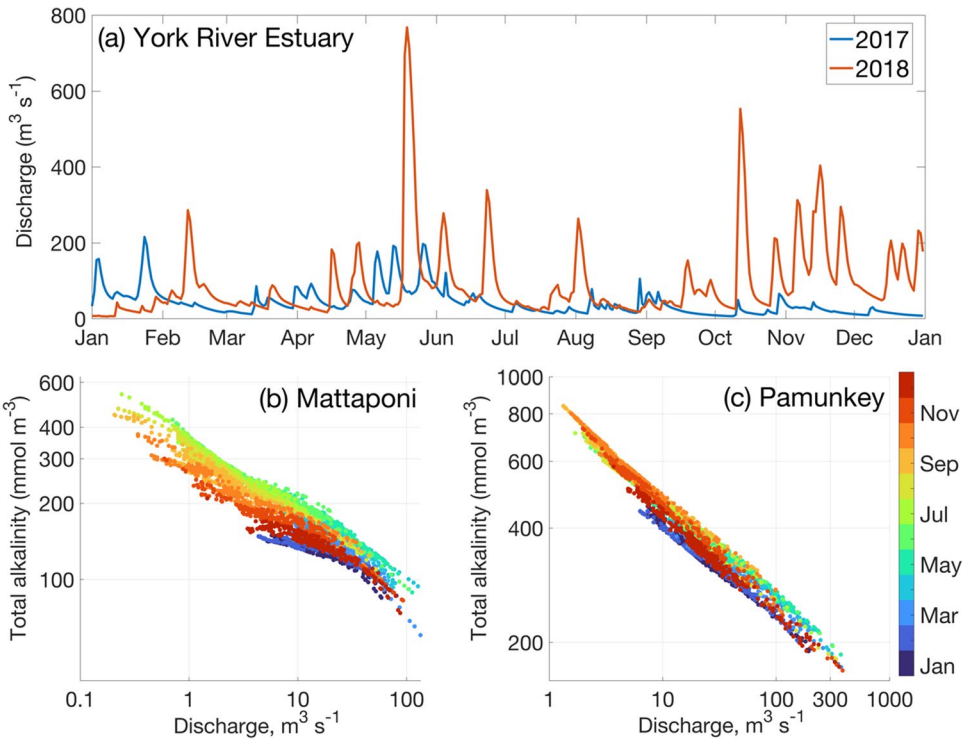

Fig. 2 **a** Time series of phase 6 Chesapeake Bay Watershed Model freshwater discharge entering the York River Estuary in 2017 and 2018, and **b**, **c** scatterplots showing relationships between historical (i.e., 1985–1993) daily observations of $\log_{10}$ (discharge) and WRTDS $\log_{10}$ (alkalinity) entering the **b** Mattaponi and **c** Pamunkey tributaries. **b** and **c** have different axis ranges, with the Pamunkey tributary having higher discharge and alkalinity concentrations

the Regional Ocean Modeling System (ROMS; Shchepetkin and McWilliams 2005) is used to study mechanisms driving the YRE carbonate system. The model domain (Fig. 1) includes the YRE and its tributaries (i.e., the Pamunkey and Mattaponi Rivers), with a horizontal resolution of 120 m and 20 stretched terrain-following vertical levels. Coastlines of the model are floodable (Warner et al. 2013), and the grid includes cells representing tidal wetlands (e.g., marshes and submerged aquatic vegetation; Fig. 1). Tidal wetlands in the YRE are fully covered by the model grid based on best estimates of wetland areas (Mitchell et al. 2017). There are 17 state variables in the ECB model (see St-Laurent et al. 2020 for the full equations and Da et al. 2021 for additional updates). In addition to O_2, temperature and salinity, this study primarily focuses on the carbon module that includes the following state variables: DIC, TA, dissolved organic carbon (DOC), and two size classes of detrital carbon. TA is dynamically controlled by sinks and sources of ammonium (NH_4^+) and nitrate (NO_3^-) associated with the water column and sediment. Because mean organic alkalinity is estimated to be only 20 mmol m^{-3} in the Chesapeake Bay (Herrmann et al. 2020), it is neglected in the model. Since submerged aquatic vegetation, a possible source of calcium carbonate in the Bay (Su et al. 2020), remains at low levels throughout most of the YRE (Moore 2009), calcium carbonate precipitation and dissolution are also assumed to be negligible. Modeled pH and pCO_2 are calculated in CO2SYS using temperature, salinity, DIC, and TA from the 3D model, assuming equilibrium constants of Cai and Wang (1998). pH is reported on the NBS scale to match the observations (see "In Situ Observations in the YRE"). Concentrations of total suspended solids (TSS) in the water column, including four inorganic and two organic particle size classes, are governed by resuspension and deposition processes dependent on shear stress. Organic particles are also subject to biogeochemical processes. The diffuse light attenuation coefficient (K_d) used in phytoplankton growth is formulated as a linear function of TSS and salinity. Additional details on the sediment transport model implemented in the present study are described in Turner et al. (2021).

Several updates have been made to the ECB module compared to previous implementations (St-Laurent et al. 2020; Da et al. 2021), so that it more accurately represents biogeochemistry in the YRE. The most significant modification involves the inclusion of TA and DIC fluxes due to net sulfate reduction in the sediments (i.e., a combination of sulfate reduction and sulfide oxidation; see Electronic Supplementary Material for details). Historical observations in the Chesapeake Bay indicate that sulfate reduction in sediment could be a dominant benthic respiration process in warmer seasons (Roden and Tuttle 1993; Marvin-DiPasquale and Capone 1998; Cai et al. 2017). Raymond et al. (2000) and Najjar et al. (2020) also suggest that sulfate reduction is an important source of TA in the YRE. Thus, in this implementation of ROMS-ECB, TA and DIC fluxes from net sulfate reduction in the estuarine sediment are added to the model's bottom vertical level. The model assumes that 70% of the decomposed particulate organic material in the seabed is associated with sulfate reduction (Mackin and Swider 1989), and one third of the sulfide produced is permanently buried (Roden and Tuttle 1993), and up to two thirds of the sulfide is reoxidized (Mackin and Swider 1989; Jørgensen 1996). As a result, TA and DIC flux from sediment is determined by the decomposition of particulate organic matter in the sediment. Additionally, the sedimentary TA:DIC ratio due to net sulfate reduction is a function of bottom oxygen concentration (Table S1).

Several additional minor updates to the model have also been made. For example, the phytoplankton parameters used in previous ROMS-ECB implementations depend on nutrient and light availability and are representative of estuarine species and are not appropriate for the fresh inland segment of this model domain. Therefore, in this implementation, the growth rate of phytoplankton is further modulated with a Michaelis–Menten function of salinity (half-saturation parameter of five salinity units) that limits growth in fresh water. This adjustment also partially offsets the impact from overestimates in light availability in low-salinity regions and improves modeled primary production. To accurately represent phytoplankton growth in freshwater (Anderson 1986; Bukaveckas et al. 2011), the model would require a new phytoplankton class dedicated to the freshwater environment; however, this is beyond the scope of this study. While groundwater TA concentrations are typically one to three times greater than those of river water (Zhang and Planavsky 2019), the global freshwater submarine discharge represents only about 1% of global river discharge (Zhou et al. 2019). Therefore, for the purposes of this study, the contributions of TA and DIC from groundwater are not explicitly included. However, because higher TA and DIC concentrations from freshwater discharge are prescribed to the model forcing when discharge is lower (see "Model Forcing"), the contribution of groundwater TA and DIC is implicitly represented in our model.

Model Forcing

Meteorological forcings are derived from ERA5 (Hersbach et al. 2023) as described in Da et al. (2021). These include winds at a 10-m height, downward long-wave and net short-wave radiation, precipitation, dewpoint temperature, and air temperature and are all at a temporal frequency of three hours and a horizontal resolution of 0.25°. Since the seasonality of atmospheric pCO_2 (± 3 µatm between 1959 and 2019 at Mauna Loa) was found to have a minimal impact on modeled daily pCO_2 at the surface; atmospheric

pCO_2 is represented by a quadratic polynomial function of time (St-Laurent et al. 2020). Along the coastline, the model receives terrestrial nitrogen, carbon, and sediment inputs derived from the Phase 6 Chesapeake Bay Watershed Model (CBPWM; Bhatt et al. 2023) and USGS data. Daily inputs from CBPWM include freshwater discharge (Fig. 2a), temperature, and concentrations of NH_4^+, NO_3^-, organic nitrogen, and sediment. Since organic carbon is not available from the CBPWM, concentrations are computed from organic nitrogen by assuming constant carbon-to-nitrogen ratios of 10:1 for DOC (Hopkinson et al 1998) and 6.625:1 (Redfield ratio) for detrital carbon, respectively. Daily riverine TA concentrations are computed from daily CBPWM freshwater discharge and monthly varying linear relationships (Table S2) between USGS historical observations of $\log_{10}$ (discharge) and WRTDS $\log_{10}$ (TA), calculated separately for the Mattaponi and Pamunkey tributaries (Fig. 2b,c). Daily DIC concentrations for model inputs are then calculated from daily riverine TA and daily DIC/TA ratios, which are linearly interpolated from the monthly climatology of USGS WRTDS DIC/TA ratios in each tributary.

Open boundary conditions along the southern, eastern, and northern edges of the model domain (Fig. 1) are generated from a 600-m resolution Bay-wide implementation of ROMS-ECB (St-Laurent and Friedrichs 2024) and observations at three CBIBS buoys. Evaluation of modeled salinity with observations from the WQMP and the CBIBS buoys reveals a small fresh bias. To improve the realism of the salinity boundary conditions, values of salinity along the three lateral boundaries are corrected by the time-averaged model bias computed at the nearest CBIBS buoy (Fig. 1). Linear relationships between surface salinity and TA measured at the York River Buoy ($TA = 37 \times S + 995$, $R^2 = 0.96$; Shadwick et al. 2019) are used to compute TA along the southern boundary. DIC concentrations are calculated from these TA concentrations and time-varying DIC/TA ratios derived from high-frequency pH data (Shadwick et al. 2019). Along the northern and eastern boundaries, linear TA vs. S relationships as well as relationships between salinity and DIC developed for the mainstem Chesapeake Bay (Friedman et al. 2020) are applied to obtain 3-hourly TA and DIC fields. These TA and DIC estimates are applied to the 3D-coupled hydrodynamic-biogeochemical model as open boundary conditions to generate 3D model simulations throughout the YRE. Henceforth, the model results discussed in this study, such as TA and DIC, pertain specifically to the outcomes obtained from the 3D model simulations described in the following section (see "Model Simulations and Skill Assessment").

The ECB module does not explicitly represent biogeochemical characteristics of tidal wetlands; therefore, lateral inputs of DON, DOC, DIC, and TA from the tidal wetland grid cells to the estuarine grid cells are parameterized. Water levels and currents in the tidal wetlands are explicitly represented by ROMS via the wetting/drying scheme of Warner et al. (2013). In this scheme, model grid cells associated with a water level that is below a given threshold are considered "dry" and no longer participate in horizontal advection or diffusion until the water levels increase again. Salinity and all other tracer concentrations associated with dry cells remain fixed until the cell is once again inundated. Rather than explicitly representing the biogeochemical processes inside the tidal wetlands (e.g., marsh growth), we opted for a simpler approach in which an "ad hoc" source of DON, DOC, DIC, and TA is implemented. The refractory-to-semilabile ratio for wetland inputs of dissolved organic matter is set to 2:1 since vascular plants such as marshes tend to produce more refractory material (Moran and Hodson 1989; Canuel and Hardison 2016), and carbon-to-nitrogen ratios are set to 20:1 and 10:1 for refractory and semilabile matter, respectively. Tidal wetlands in the YRE are typically a sink of particulate organic matter (Knobloch et al. 2021) and dissolved inorganic nitrogen (Neubauer et al. 2005); therefore, particulate organic nitrogen and carbon as well as dissolved inorganic nitrogen are not included as inputs from the tidal wetlands. This ad hoc source is uniform over the area of the tidal wetlands and has a seasonal cycle that decreases the mean amplitude in the winter and increases it in the summer (Fig. S1), mimicking the seasonality of wetland gross primary production (GPP) of Feagin et al. (2020). The ad hoc source is only active over tidal wetland grid cells that are inundated at each model time step.

The ad hoc source to the tidal wetlands is further modified by the estuarine biogeochemical equations of the model (which are active inside the wetlands even though they are not necessarily representative of wetland vegetation). For example, the estuarine biogeochemical equations include the air-sea CO_2 flux that effectively outgasses a substantial fraction of the DIC being introduced by the ad hoc source. This modified ad hoc source results in a lateral flux of DON, DOC, DIC, and TA, directed from the tidal wetlands to the estuary when wetland grid cells are inundated, and concentration gradients are positive. Since there is considerable uncertainty associated with the magnitude of the observed DON, DOC, DIC, and TA inputs to the estuary from the wetlands, values of ad hoc sources are selected such that they provide reasonable estuarine model skill near the wetlands (e.g., the Sweet Hall March CONMON station) and are consistent with the large range of values reported in the literature (Neubauer and Anderson 2003; Najjar et al. 2018; Yau et al. 2022; Reithmaier et al. 2023). The annual mean values of the added ad hoc sources are 1.2, 18.2, 46.8, and 8.0 mmol m^{-2} day^{-1} for DON, DOC, DIC, and TA, respectively. Ultimately, the quantity that is scientifically relevant for the present study is the lateral flux directed from these

"parameterized wetlands" to the estuary. Hereafter, this key quantity, representing wetland inputs of DIC and TA, is reported as annual mean values and time series in the results.

Model Simulations and Skill Assessment

A reference simulation is conducted for January 2017 through December 2018, as this includes average (2017) and high (2018) river flow conditions (Fig. 2a). A sensitivity experiment is conducted for these two years to investigate the impact of tidal wetlands on the YRE carbonate system. In this sensitivity experiment, both wetland grid cells and the empirical DIC and TA inputs from tidal wetlands, as described in "Model Forcing", are removed. As a result, this experiment simulates "no wetland" and "no flooding" conditions, providing a bias assessment associated with the omission of tidal wetlands in studies of estuarine carbonate systems conducted with numerical models. A one-year spin-up (i.e., conducting a 2017 simulation twice) is included for the reference simulation and the sensitivity experiment, which is substantially longer than the two- to three-month residence time of the YRE (Shen and Haas 2004).

Results from the reference simulation are compared with CONMON and WQMP water quality data (see "In Situ Observations in the YRE"). This study focuses specifically on the evaluation of temperature, salinity, O_2, and pH throughout the YRE. Daily mean model results are compared to daily mean CONMON data at the same depth (~ 1 m). Modeled variables matching the specific times and depth when WQMP data were collected are used for point-to-point comparisons throughout the water column. In addition, the TA and DIC estimates obtained using CO2SYS are compared to the 3D model results, though the errors inherent in the estimated TA and DIC concentrations are acknowledged. Quantitative skill metrics (Table 1) include mean, model bias, and root-mean squared difference (RMSD). Furthermore, modeled GPP is compared to data-driven estimates of pelagic GPP calculated from chl-a data (Qin and Shen 2019). Modeled GPP specifically refers to pelagic GPP associated with phytoplankton growth in the water column. To evaluate ecosystem GPP, additional primary producers such as seagrass and benthic algae would need to be included in the model, which could be addressed in a future study. Additionally, modeled TSS and K_d are compared to WQMP data to evaluate the light availability in the model.

DIC and TA Budgets

Based on the model simulations described above, budgets over the estuarine grid cells (i.e., excluding tidal wetlands) are computed for DIC and TA and include terms representing net horizontal advection (*hadv*), biological processes (*bio*), and CO_2 exchange with the atmosphere (*atm*; for DIC only). The vertically integrated (surface to bottom) DIC and

Table 1 Summary of model skill metrics

Variable		Mean ± standard deviation		Bias	Unbiased RMSD[c]	RMSD
		Model	*Observation/estimate*			
Temperature (°C)	W[a]	18.0 ± 8.3	17.9 ± 8.4	0.1	− 1.2	1.2
	C[b]	17.6 ± 8.7	17.4 ± 8.7	0.1	− 1.2	1.2
Salinity	W	16.1 ± 6.8	16.1 ± 5.8	− 0.0	2.2	2.2
	C	10.7 ± 8.4	11.0 ± 8.1	− 0.3	1.5	1.5
Oxygen (mmol m^{-3})	W	251 ± 69	239 ± 81	12	− 35	37
	C	288 ± 50	258 ± 72	29	− 39	49
pH (NBS)	W	7.8 ± 0.4	7.7 ± 0.4	0.1	0.2	0.2
	C	7.7 ± 0.5	7.6 ± 0.5	0.1	0.2	0.2
TA (mmol m^{-3})	W	1499 ± 403	1504 ± 376[d]	− 4.6	121.4	121.5
	C	1131 ± 533	1170 ± 530[d]	− 39.0	112.9	119.5
DIC (mmol m^{-3})	W	1457 ± 351	1501 ± 349[e]	− 44.2	121.7	129.4
	C	1131 ± 458	1206 ± 444[e]	− 75.0	138.5	157.5

[a]W refers to discrete Water Quality Monitoring Program data collected at seven stations (Fig. 1) throughout the water column over the years 2017–2018

[b]C refers to daily mean Continuous Monitoring data collected at six stations (Fig. 1) at roughly 1-m-depth over the years 2017–2018

[c]RMSD refers to root-mean-squared difference. Unbiased RMSD represents the RMSD after removing the mean (Jolliff et al. 2009)

[d]Since TA observations are not available, estimates are calculated from in situ salinity observations and a linear TA vs. salinity relationship

[e]Since DIC observations are not available, estimates are derived from TA estimates together with in situ observations of pH, temperature, and salinity

TA budgets are calculated for each model time step and averaged over a desired period (i.e., daily or annual averages with units of mmol day^{-1} or mmol year^{-1}, respectively):

$$\frac{\partial}{\partial t}\iiint [\mathrm{DIC}]\,\mathrm{dV} = F_{\mathrm{hadv}}^{\mathrm{DIC}} + F_{\mathrm{bio}}^{\mathrm{DIC}} + F_{\mathrm{atm}}^{\mathrm{DIC}} \quad (1)$$

$$\frac{\partial}{\partial t}\iiint [\mathrm{TA}]\,\mathrm{dV} = F_{\mathrm{hadv}}^{\mathrm{TA}} + F_{\mathrm{bio}}^{\mathrm{TA}} \quad (2)$$

[DIC] and [TA] represent concentrations, and the terms on the left-hand side of Eqs. (1) and (2) are changed in DIC and TA inventory over time. The terms on the right-hand side are flux of DIC and TA due to each process. The net horizontal advection term is the sum of inputs at the lateral boundaries of the estuary, i.e., from rivers (*riv*), wetland cells (*wet*), and the YRE mouth connected to the mainstem of the Chesapeake Bay (*bay*, see Fig. 1):

$$F_{\mathrm{hadv}}^{\mathrm{DIC}} = F_{\mathrm{riv}}^{\mathrm{DIC}} + F_{\mathrm{wet}}^{\mathrm{DIC}} + F_{\mathrm{bay}}^{\mathrm{DIC}} \quad (3)$$

$$F_{\mathrm{hadv}}^{\mathrm{TA}} = F_{\mathrm{riv}}^{\mathrm{TA}} + F_{\mathrm{wet}}^{\mathrm{TA}} + F_{\mathrm{bay}}^{\mathrm{TA}} \quad (4)$$

Biological sources and sinks of DIC ($F_{\mathrm{bio}}^{\mathrm{DIC}}$) include GPP ($F_{\mathrm{PP}}^{\mathrm{DIC}}$) and respiration ($F_{\mathrm{resp}}^{\mathrm{DIC}}$):

$$F_{\mathrm{bio}}^{\mathrm{DIC}} = F_{\mathrm{PP}}^{\mathrm{DIC}} + F_{\mathrm{resp}}^{\mathrm{DIC}} \quad (5)$$

Note that $F_{\mathrm{PP}}^{\mathrm{DIC}}$ is always negative (a sink of DIC), whereas $F_{\mathrm{resp}}^{\mathrm{DIC}}$, which represents sources of DIC from both aerobic and anaerobic respiration, is always positive. Net ecosystem production (NEP) is defined as $-F_{\mathrm{bio}}^{\mathrm{DIC}}$, such that when $\left|F_{\mathrm{PP}}^{\mathrm{DIC}}\right| < \left|F_{\mathrm{resp}}^{\mathrm{DIC}}\right|$ then NEP < 0, and the system is net heterotrophic. Biological sources and sinks of TA include not only production ($F_{\mathrm{PP}}^{\mathrm{TA}}$), and respiration ($F_{\mathrm{resp}}^{\mathrm{TA}}$) but also nitrification ($F_{\mathrm{nitrif}}^{\mathrm{TA}}$):

$$F_{\mathrm{bio}}^{\mathrm{TA}} = F_{\mathrm{PP}}^{\mathrm{TA}} + F_{\mathrm{resp}}^{\mathrm{TA}} + F_{\mathrm{nitrif}}^{\mathrm{TA}} \quad (6)$$

$F_{\mathrm{PP}}^{\mathrm{TA}}$ denotes TA changes due to phytoplankton uptake of both NO_3^- and NH_4^+ ($F_{\mathrm{PP}}^{\mathrm{TA}} = F_{\mathrm{PP\_NO3}}^{\mathrm{TA}} + F_{\mathrm{PP\_NH4}}^{\mathrm{TA}}$); $F_{\mathrm{resp}}^{\mathrm{TA}}$ is always a source of TA, and it includes aerobic and anaerobic respiration in the water column and sediment. In the water column, aerobic respiration of organic matter increases TA by generating NH_4^+, and denitrification increases TA by consuming NO_3^-. In the model's sediment, aerobic respiration and coupled nitrification–denitrification together amounts to a net yield of 4 mol NH_4^+ and 6 mol N_2 from the decomposition of 1 mol of organic matter (Fennel et al. 2006). Additionally, net sulfate reduction in the sediment contributes to TA production, depending on bottom organic matter and oxygen levels (see Electronic Supplementary Material for details; Table S1). Nitrification and phytoplankton uptake of NH_4^+ are the only sinks of TA in the model.

The above DIC and TA budgets are presented in three formats. In the first two formats, volume integrals of each term are calculated across the entire estuary at every model time step. Subsequently, the results are averaged over a year to produce annual mean budgets (10^9 mmol year^{-1}, i.e., Mmol year^{-1}) and over a day to yield daily time series (mmol day^{-1}). The third format presents volume averages across the main axis of the Pamunkey–York River portion of the estuary, which is divided into 82 regions with similar surface areas. Since the Mattaponi River is a much smaller tributary than the Pamunkey River, the former is not considered in volume-averaged budgets. For each region, budgets are first calculated via Eqs. (1) to (6), and then scaled by annual mean regional volumes to obtain volume averages (mmol m^{-3} day^{-1}). These three types of DIC and TA budgets are computed in 2 years (2017 and 2018) representing contrasting flow conditions (Fig. 2a), to investigate the substantial year-to-year variability that is common in the YRE. These budgets are computed for both the reference simulation and the sensitivity simulation with no tidal wetlands. Unless otherwise noted, absolute values are used when reporting changes in budget terms that are negative. To investigate the impacts of tides on processes controlling DIC and TA, tidal energy flux is also computed (Taylor 1920). Three-hourly time series of tidal energy flux entering the mouth of the YRE is calculated from water depth, free surface elevation, vertically averaged velocity, and width of the river mouth.

Results

Model-Data Comparison

The evaluation of model performance with WQMP and CONMON observations shows that temperature, salinity, O_2, and pH data are reasonably well reproduced by the model throughout the YRE (Table 1; Fig. S2). Temperature and salinity show only a small model bias (0.1 °C and up to −0.3 units, respectively) and a low RMSD (~ 1.2 °C and 1.5–2.2 units, respectively). Modeled O_2 concentrations are biased high by 12 to 29 mmol m^{-3} throughout the YRE, which is likely due to biases in biological processes. A recent modeling study (Cai et al. 2023) showed that simulating the metabolism of tidal marshes helps capture low-O_2 events related to enhanced respiration at night. The present study does not include impacts of tidal wetlands on O_2, which may be why O_2 is overestimated at stations adjacent to extensive tidal marshes (e.g., Whitehouse Landing, Sweet Hall Marsh and Taskinas Creek; Fig. S3). Modeled pH has a positive bias of 0.1 pH units and an RMSD of 0.2 pH units over the 2 years examined;

this agreement is as high as can be expected, given that the observed pH comes with a relatively low precision of ± 0.2 pH units (see "In Situ Observations in the YRE"). In addition, the same model-data comparisons are performed for the sensitivity experiment that excludes wetland grid cells and the associated empirical inputs. At stations in the York River, the spatial and temporal patterns of temperature and salinity are well captured even without tidal wetlands. However, the sensitivity experiment underestimates salinity at Sweet Hall Marsh (Fig. S3) compared to the reference run and observations, suggesting that including wetland grid cells enhances saltwater intrusion into the Pamunkey River.

Since observed TA and DIC concentrations are unavailable, 3D model results are compared to TA and DIC products estimated using a linear TA vs. S relationship (see "In Situ Observations in the YRE"). Model results are consistent with the spatial and temporal patterns of these estimated TA and DIC concentrations (Fig. S4). Both the derived TA and DIC products and the 3D model concentrations range from 500 mmol m^{-3} at the head of the Pamunkey to 1900 mmol m^{-3} at the mouth of the estuary. On average, however, the 3D model produces slightly lower values (lower by 4.6 to 39 mmol m^{-3} for TA and lower by 44 to 75 mmol m^{-3} for DIC; Table 1). These differences in DIC are consistent with the positive bias in modeled O_2 concentrations and are similarly located in the upper tributaries, suggesting that the model also may be underestimating aerobic respiration associated with tidal marshes. Compared to the reference run and the estimated data products, TA and DIC are both lower at Sweet Hall Marsh in the sensitivity experiment without tidal wetlands (Fig. S4). The improvements shown in the reference run are due to enhanced saltwater intrusion and the added wetland inputs of TA and DIC. It is possible that wetland inputs partially mask the bias in modeled TA and DIC inherited from other model limitations. However, identifying such biases is challenging without in situ observations of the carbonate system in estuarine waters and nearby tidal marsh porewaters.

The model captures the magnitude and variability of pelagic GPP, TSS, and K_d reasonably well, although bias exists in low-salinity waters (Fig. S5, S6). As in the data-based estimates of pelagic GPP from Qin and Shen (2019), our modeled annual mean GPP increases downstream, with maximum GPP rates of 0.9 ± 1.5 g C m^{-2} day^{-1} (mean ± standard deviation) near the mouth of the YRE (Fig. S5). The model, however, underestimates GPP in the tidal fresh region, where the implementation of a separate freshwater phytoplankton class could be explored in the future. Since tidal fresh regions cover less than 10% of the total surface area of the YRE, and the pelagic GPP rate is 1/3 of the rate at saline sites (Qin and Shen 2019), their contribution to total estuarine pelagic GPP is minimal. In addition, modeled TSS concentrations and surface K_d agree reasonably well with observations, especially in the York portion of the estuary (Fig. S6). In the lower Pamunkey River, where observed TSS has large temporal variability, the model tends to underestimate observed TSS concentrations, which may be partially due to the comparison of daily averaged model values with observed TSS snapshots.

Annual Mean DIC and TA Budgets

Both physical and biogeochemical processes substantially contribute to the overall DIC budget in the YRE (Fig. 3a).

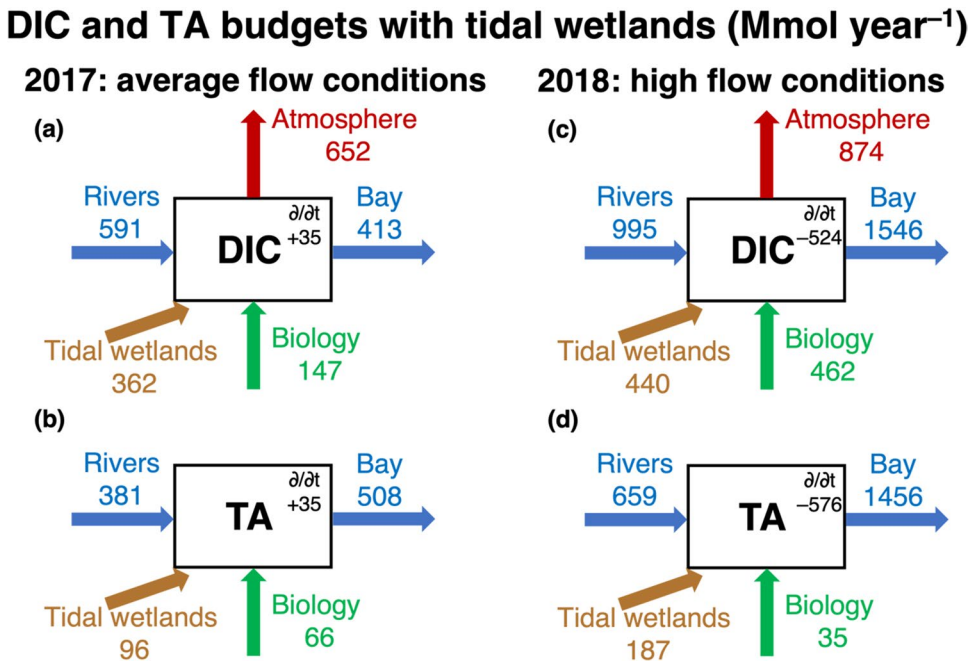

Fig. 3 Annual mean dissolved inorganic carbon (DIC) and total alkalinity (TA) budgets of the York River Estuary in 2017 (**a**, **b**) and 2018 (**c**, **d**). Arrows represent sources and sinks associated with rivers, tidal wetlands, net biology, advection to the Chesapeake Bay, and outgassing to atmosphere (for DIC only). The annual mean DIC and TA time tendency term is given by ∂/∂ t. All budgets are closed (with the small mismatch caused by rounding errors). Note that 1 Mmol $year^{-1}$ represents 10^9 mmol $year^{-1}$

In the normal flow year (2017), inputs of DIC from rivers and wetlands account for nearly one half and one third, respectively, of the total DIC inputs to the YRE, with biological processes being a relatively weak source of DIC (Fig. 3a). However, DIC changes due to GPP (F_{PP}^{DIC}) and respiration (F_{resp}^{DIC}) individually, the two terms contributing to F_{bio}^{DIC}, are four to seven times larger than the other sources and sinks of DIC (Table 2). On average, respiration is greater than production indicating the system is net heterotrophic (NEP = −147 Mmol year^{-1}). CO_2 evasion to the atmosphere and lateral advection of DIC at the YRE mouth explain roughly 60% and 40% of the total DIC sink, respectively. Overall, total inputs of DIC nearly balance total exports, resulting in a small positive ∂/∂t term.

As is the case for DIC, in the average flow year of 2017, the TA budget is controlled by both physical and biogeochemical processes (Fig. 3b). River inputs of TA account for 70% of the total inputs, with TA inputs from tidal wetlands and net biology playing less important roles. However, the biological term includes changes in TA due to GPP, respiration, and nitrification, all three of which are individually comparable in magnitude to river inputs of TA (Table 2). This is in direct contrast to the DIC budget where the individual biological terms were many times greater than the riverine inputs. Specifically, F_{PP}^{TA} is a sink because TA losses via NH_4^+ uptake by phytoplankton generally exceed the TA gains via NO_3^- uptake (Table 2). F_{resp}^{TA} is a large source due to the release of NH_4^+ via water column respiration and sedimentary production of TA. F_{nitrif}^{TA} is a smaller sink of TA due to NH_4^+ consumption and NO_3^- production. The inputs of TA from rivers, wetlands, and biological processes are balanced by the export of TA to the main stem Chesapeake Bay, resulting in a small change in TA with respect to time, as was the case for DIC. On an annual basis, these total TA inputs (from rivers, wetlands, and biological process) are roughly half of the total DIC inputs (Fig. 3; DIC/TA ratio of inputs from rivers, wetlands, and biological processes are 1.6, 3.8, and 2.2, respectively); in contrast, DIC/TA ratio of the export flux is much lower (0.8).

In 2018, when freshwater discharge is 118% higher than in the average flow conditions of 2017, most sources and sinks of DIC and TA are substantially higher, and the system is even more net heterotrophic (NEP = −462 Mmol year^{-1}). Riverine DIC and TA fluxes increase by 70% (Fig. 3c, d). Inputs of DIC and TA from tidal wetlands are both higher than those in 2017 by ~ 80–90 Mmol year^{-1}. This is a result of decreased DIC and TA concentrations in the estuary, which increases the concentration gradients between the estuarine and wetland grid cells. Compared to the average flow conditions of 2017, the biological source of DIC is 315 Mmol year^{-1} higher in 2018, 80% of which (Table 2) is due to decreases in GPP and 20% due to increases in respiration. In contrast, the overall biological source of TA is lower in 2018 compared to 2017, mainly due to a nearly 50% increase in nitrification (F_{nitrif}^{TA}) of 68 Mmol year^{-1}, though this is partially offset by decreases in production and respiration (Table 2). CO_2 evasion to the atmosphere is 34% higher in 2018 than 2017, while increases in DIC and TA exports to the Bay are even greater (274% and 187%, respectively). Although the total lateral inputs of DIC and TA from rivers and tidal wetlands nearly double in 2018, the exports to

Table 2 Annual mean DIC and TA budgets in the average flow conditions of 2017 and high flow conditions of 2018 for the reference simulation (ref) and in the sensitivity simulation without wetlands and flooding (w/o)

Year	DIC budget (Mmol year^{-1})							TA budget (Mmol year^{-1})						
	F_{PP}^{DIC}	F_{resp}^{DIC}	F_{atm}^{DIC}	F_{riv}^{DIC}	F_{wet}^{DIC}	F_{bay}^{DIC}	$\frac{\partial DIC}{\partial t}$	F_{PP}^{TA}		F_{resp}^{TA}	F_{nitrif}^{TA}	F_{riv}^{TA}	F_{wet}^{TA}	F_{bay}^{TA}	$\frac{\partial TA}{\partial t}$
								$F_{PP\_NO3}^{TA}$	$F_{PP\_NH4}^{TA}$						
2017 ref	−2523	2670	−652	591	362	−413	35	−236		457	−155	381	96	−508	35
								72	−308						
2017 w/o	−2779	2769	−192	591	0	−387	1	−265		502	−134	381	0	−482	2
								77	−342						
2018 ref	−2270	2732	−874	995	440	−1546	−524	−207		465	−223	659	187	−1456	−576
								68	−275						
2018 w/o	−2651	2961	−452	995	0	−1371	−518	−242		527	−203	659	0	−1324	−582
								79	−321						

Positive and negative values refer to sources and sinks of DIC (or TA), respectively. Subscripts in DIC budget terms represent flux due to biological processes, including primary production (*PP*) and respiration (*resp*); flux due to air-sea gas exchange (*atm*); and flux at the lateral boundaries of the estuary, i.e., from rivers (*riv*), tidal wetlands (*wet*), and the YRE mouth connected to the mainstem of the Chesapeake Bay (*bay*). The sum of the three terms at the lateral boundaries represents net horizontal advection (see "Method"). Identical subscripts are used in the TA budget, with an extra term for nitrification (*nitrif*). Additionally, TA flux due to primary production is separated into phytoplankton uptake of NO_3^- (*PP_NO3*) and NH_4^+ (PP_NH4)

the Chesapeake Bay increase by approximately three times, as reflected by the negative time rates of change ($\partial DIC/\partial t = -524$ and $\partial TA/\partial t = -576$ Mmol year^{-1}; Fig. 3c,d).

As expected in the sensitivity simulation without wetlands, total inputs and exports of DIC and TA are lower (Fig. 4; Table 2). When wetlands are not included in the simulation, reductions in biological DIC sources (by −157 and −152 Mmol year^{-1} in 2017 and 2018, respectively; Fig. 4) are caused by increases in GPP exceeding increases in respiration (Table 2). While biological processes are a net source of DIC when wetlands are included (i.e., net heterotrophy; Fig. 3a,b), in the simulation without wetlands, biological processes represent a small sink indicating weak net autotrophy in 2017 (NEP = +10 Mmol year^{-1}; Table 2) and a smaller source (weak net heterotrophy; NEP = −10 Mmol year^{-1}; Table 2) in 2018 (Fig. 4). Without wetlands, CO_2 evasion to the atmosphere is 71% and 48% lower in 2017 and 2018, respectively. Decreases in DIC exports to the Bay are also smaller, in terms of both percent and absolute magnitude. In terms of the TA budget without wetlands (Fig. 4c,d), decreases in export to the Bay are similar to those of DIC. While the total inputs of TA are smaller without wetlands, biological processes become a slightly stronger source of TA due to a combination of changes in GPP (−29 Mmol year^{-1}), respiration (+45 Mmol year^{-1}), and nitrification (+21 Mmol year^{-1}) for 2017, with similar patterns shown in 2018.

Temporal Variability of DIC and TA Sources and Sinks

Sources and sinks of DIC in the YRE exhibit strong temporal variability on seasonal and quasi-monthly scales (Fig. 5). DIC losses due to GPP and DIC gains due to respiration both show strong seasonal cycles with greatest values in the summer (Fig. 5a), primarily driven by light and temperature, while their sum (F_{bio}^{DIC}) has no clear seasonal variability. CO_2 outgassing (F_{atm}^{DIC}) is greater both in warmer seasons, as expected from impacts on solubility, and during high river discharge events. Superimposed on the seasonal cycles in F_{PP}^{DIC}, F_{bio}^{DIC}, and F_{atm}^{DIC} are quasi-monthly tidal oscillations (periodicity of 27.5 days). Positive F_{bio}^{DIC} values generally occur when the tidal energy flux is stronger. F_{bio}^{DIC} also fluctuates between positive and negative values with the tidal cycle except during high discharge events when F_{bio}^{DIC} is consistently positive (e.g., Oct–Nov 2018). The spike in F_{bio}^{DIC} in May 2018 is due to a simultaneous reduction in GPP associated with high tidal energy flux and an increase in respiration associated with increased river input. The number of days of net autotrophy vs. heterotrophy is 147 vs. 218 days in 2017 and 96 vs. 269 days in the wetter year of 2018. F_{wet}^{DIC} also exhibits strong seasonal variability with a summer peak (Fig. 5b) and partially contributes to the high values of F_{hadv}^{DIC} in the summer (Fig. 5c). Finally, export to the Chesapeake Bay (F_{bay}^{DIC}) becomes a greater sink of DIC in the YRE (Fig. 5c) when F_{riv}^{DIC} is greater (Fig. 5b).

Strong temporal variability is similarly found in TA sources and sinks (Fig. 6). TA losses due to GPP and nitrification, as well as TA gains due to total respiration, all show strong seasonal variability, again with greatest values in the summer (Fig. 6a) and the sum of all of these processes (F_{bio}^{TA}) exhibiting relatively weak seasonality. As is the case for F_{bio}^{DIC}, the quasi-monthly variability due to the tidal energy flux is strong in F_{bio}^{TA} and F_{nitrif}^{TA}. Unlike F_{PP}^{DIC} (Fig. 5a), the quasi-monthly tidal variability in F_{PP}^{TA} is less apparent due to the counterbalance between NH_4^+ and

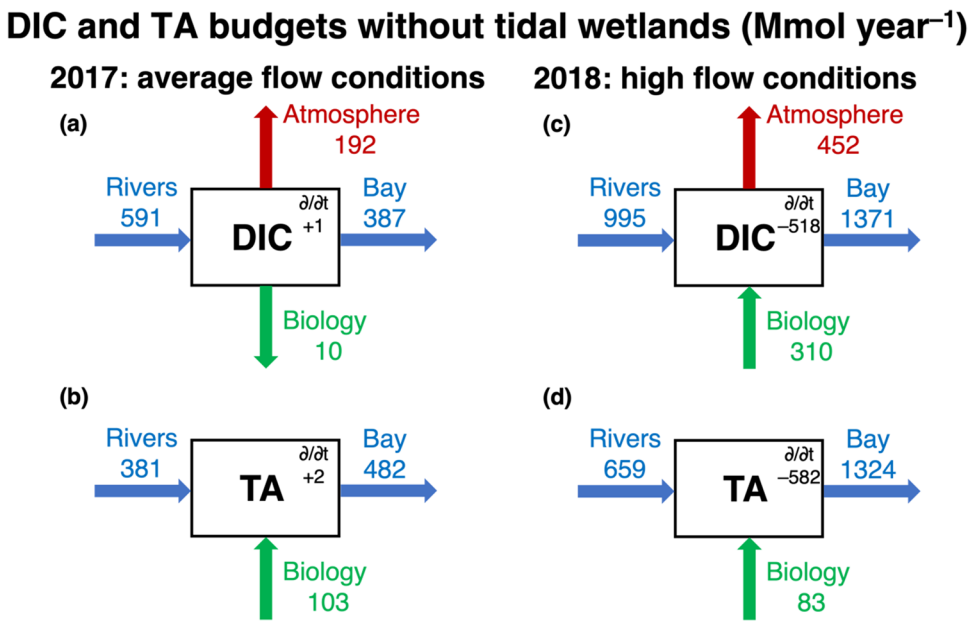

Fig. 4 As in Fig. 3, except for the simulation without tidal wetlands

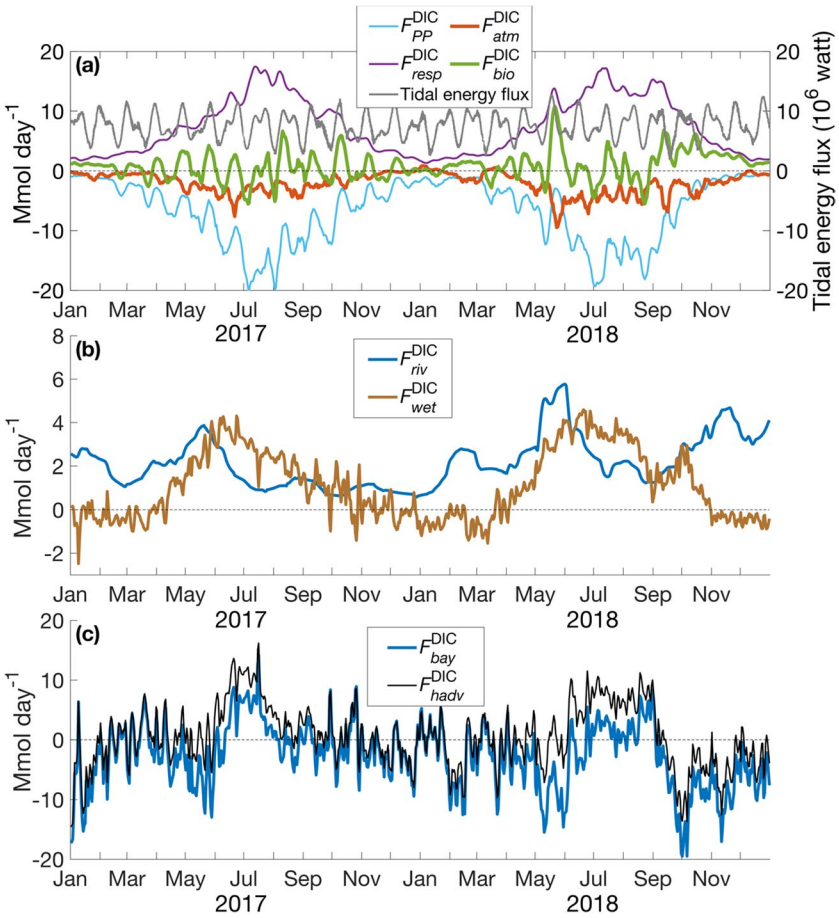

Fig. 5 Temporal variability of **a** F^{DIC}_{PP}, F^{DIC}_{resp}, F^{DIC}_{bio}, F^{DIC}_{atm}, and tidal energy flux (7-day moving averages), **b** F^{DIC}_{riv} and F^{DIC}_{wet} (30-day moving averages), and **c** F^{DIC}_{bay} and F^{DIC}_{hadv} (30-day moving averages). The *y*-axis range is different in **b** than **a** and **c**. Positive and negative values represent sources and sinks of DIC, respectively

NO_3^- uptake by phytoplankton. Increased F^{TA}_{resp} and decreased F^{TA}_{PP} both contribute to greater F^{TA}_{bio} during high river discharge events (e.g., May 2018), which is partially offset by increased F^{TA}_{nitrif}. This increase in F^{TA}_{nitrif} may even result in consistently negative F^{TA}_{bio} when river discharge remains at a high level (e.g., Oct–Nov 2018). Seasonal variability of the advective terms is relatively weak, with a slightly greater source of TA from wetlands in the summer and fall (Fig. 6b). As is the case for DIC, the tidally averaged temporal variability in fluxes from wetlands is comparable to that of TA fluxes from rivers (Fig. 6b). Additionally, the TA flux from rivers reflects the variability in freshwater discharge, with stronger river discharge driving a stronger sink flux of TA at the mouth of the estuary (Figs. 6b,c and 2a).

Spatial Variability of DIC and TA Sources and Sinks

Sources and sinks of DIC vary along the YRE (Fig. 7). The net difference between upstream inputs and downstream outputs of DIC (F^{DIC}_{hadv}) reflects the magnitude of the DIC sources and sinks within the YRE and is generally greater when and where the F^{DIC}_{atm} and F^{DIC}_{bio} terms are more negative. Net horizontal advection is a strong DIC source in the Pamunkey River (< 0 km; Fig. 7a, f) and the upper YRE (0–15 km) especially in the spring and summer, with maximum values of 25 mmol C m^{-3} day^{-1} in both average and high flow conditions. CO_2 outgassing is a strong DIC sink in the Pamunkey (–30 mmol C m^{-3} day^{-1}), which decreases rapidly downstream (Fig. 7b, g). Only in the high discharge year does outgassing increase again near West Point (i.e., 0 km in Fig. 7g). Interestingly, CO_2 influx from the atmosphere is shown to be a small source of DIC in the lower YRE in both the normal and high flow years (Fig. 7b, g). Biological processes are primarily sources of DIC throughout the YRE, except in the spring and summer when they are a weak DIC sink downstream of West Point (Fig. 7c, h). During these seasons, GPP and respiration are greatest in this region (Fig. 7d, e, i, j), where GPP typically slightly exceeds respiration (net autotrophy). In the Pamunkey (Fig. 7d, e, i, j) and the Mattaponi (not shown), respiration exceeds GPP all year long, particularly in the wetter year. Overall, the spatiotemporal patterns of these

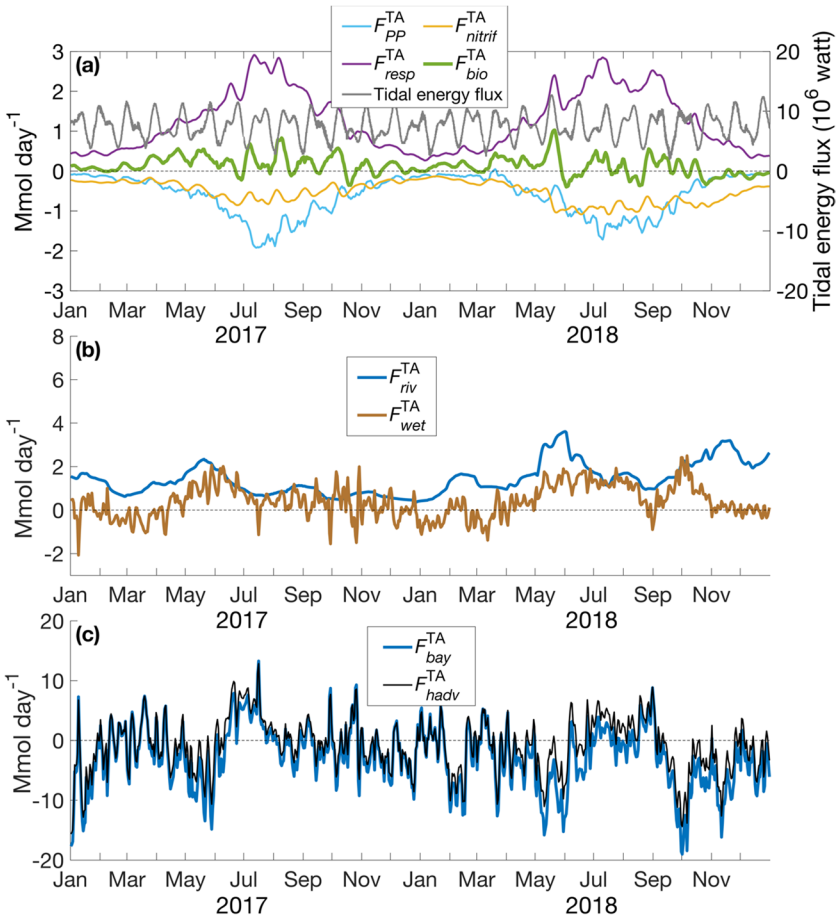

Fig. 6 Temporal variability of **a** F^{TA}_{PP}, F^{TA}_{resp}, F^{TA}_{nitrif}, F^{TA}_{bio}, and tidal energy flux (7-day moving averages), **b** F^{TA}_{riv} and F^{TA}_{wet} (30-day moving averages), and **c** F^{TA}_{bay} and F^{TA}_{hadv} (30-day moving averages). The *y*-axis range differs in the three panels. Positive and negative values represent sources and sinks of TA, respectively

fluxes are similar under average and high-flow conditions; however, the high CO_2 outgassing as well as the biological production and respiration terms extend farther downstream by 10–20 km in the wetter year (Fig. 7h, i, j).

The spatial variability of TA sources and sinks is generally smaller than that of DIC (Fig. 8). In both years, net horizontal advection is a source of TA in most of the Pamunkey (< 0 km) and the York River (> 0 km) in the summer, with a peak of 13 mmol m^{-3} day^{-1} just downstream of West Point (Fig. 8a, f). Unlike DIC, TA has spatial variability in net biological processes that is much smaller than that of net horizontal advection (Fig. 8b, g vs. a, f). Specifically, F^{TA}_{bio} has a distinct three-division pattern along the estuary (Fig. 8b, g). In the upper Pamunkey where respiration is a primary source (Fig. 8e, j), F^{TA}_{bio} reaches its maximum and is a TA source all year round. Farther downstream, the combined TA losses from GPP (Fig. 8d, i) and nitrification (Fig. 8c, h) exceed TA gains via respiration (Fig. 8e, j), resulting in a weak net TA sink. In the lower YRE, the opposite is true. We see these same spatial patterns in both years examined; however, they migrate downstream with the wetter conditions in 2018 compared to 2017.

Discussion

Estuarine Net Ecosystem Production

Both physical and biogeochemical drivers strongly influence net ecosystem production in estuaries. Unlike the Chesapeake Bay as a whole which has long been reported to be net autotrophic (Kemp et al. 1997; Herrmann et al. 2015; Feng et al. 2015; Shen et al. 2019; St-Laurent et al. 2020), this study suggests that the YRE is net heterotrophic on annual time scales, which is also consistent with Raymond et al. (2000). Other tidal estuaries of the Chesapeake Bay, such as the James River Estuary (Bukaveckas 2022) and the Rappahannock River Estuary (Hornberger et al. 1977), have also been found to be net heterotrophic. Still, other Chesapeake Bay tributaries, such as the Patuxent River Estuary, fluctuate from year to year between net heterotrophy and autotrophy (Kemp and Testa 2011).

The model experiments conducted in this study demonstrate that tidal wetlands are largely responsible for net heterotrophy in the YRE. In both the drier and wetter years, net heterotrophy increases by ~ 150 Mmol C year^{-1} due to tidal

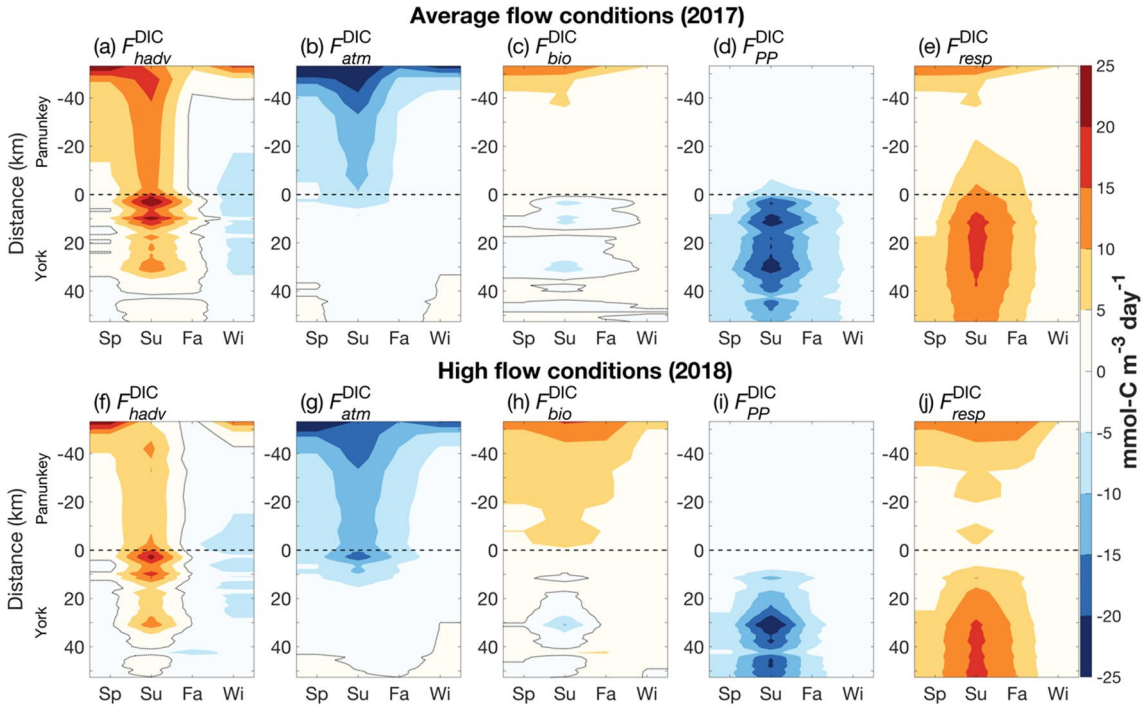

Fig. 7 Volume averaged DIC sources and sinks along the Pamunkey-York axis of the YRE in spring (Sp: March–May), summer (Su: June–August), fall (Fa: September–November), and winter (Wi: December–February). The horizontal dashed line represents West Point (i.e., the location of the convergence between the Pamunkey and York). Negative distances correspond to the Pamunkey River; positive distances correspond to the York River. **a**–**e** 2017 and **f**–**j** 2018

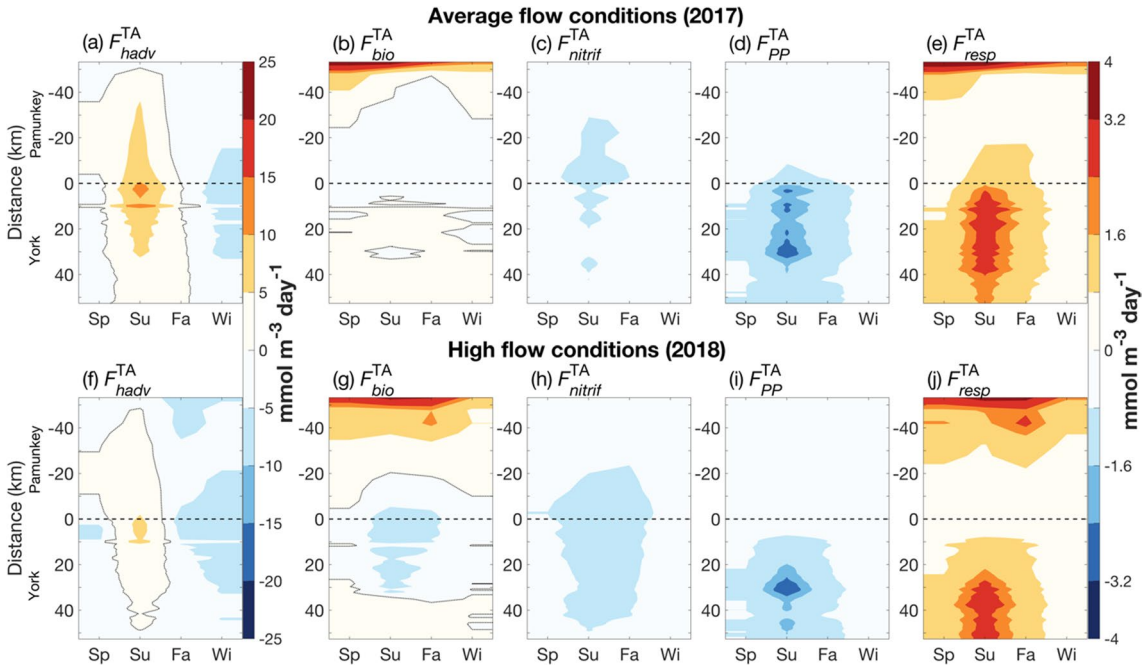

Fig. 8 As in Fig. 7, except for TA. Note the different color bar range used in **a** and **f** compared to other panels

wetlands, which is roughly equal to half of the difference between the wet and dry years examined (Figs. 3 and 4). This increased net heterotrophy occurs because the tidal wetlands reduce modeled estuarine GPP, yet have only a small effect on respiration (Table 2). The reduction in estuarine GPP is primarily driven by increased light limitation when wetlands are included in the model (Fig. S7). The inclusion of marsh area allows more oceanic water to flow into the model domain and increases bottom shear stress by increasing tidal discharge and current velocity (Friedrichs 1995) in the estuarine grid cells. Higher bottom shear stress increases sediment resuspension and light limitation and decreases estuarine GPP. Since not all autochthonous organic matter is decomposed locally, respiration changes less than GPP. These results highlight that estuarine NEP will likely be overestimated without an accurate representation of marsh area in 3D ecosystem models. In addition to the impact of TSS on light availability, marsh-derived colored DOC also absorbs light. According to Clark et al. (2020), marsh-derived colored DOC decreases light availability, which may limit phytoplankton growth in the estuary. Although DOC from marshes is parameterized in this study, we do not model its impact on light availability. This should be implemented in our model in the future to address the effects of marsh-derived colored DOC on modeled GPP in the estuary.

Terrestrial inputs, including freshwater, sediment, and nutrient loading, also substantially impact the GPP component of NEP (Henderson and Bukaveckas 2022; Bukaveckas et al. 2020; Qin and Shen 2019). An empirical model of estuarine NEP as a function of organic carbon and inorganic nitrogen inputs (Kemp et al. 1997; Herrmann et al. 2015) applied to United States estuaries revealed mostly net heterotrophy (Windham-Myers et al. 2018; Najjar et al. 2018). From the drier year to the wetter in our YRE simulations, about 80% of the tripled net heterotrophy (Fig. 3a,c; Table 2) is due to decreases in GPP associated with enhanced flushing and light limitation (e.g., Paerl and Huisman 2008; Lucas et al. 2009; Peierls et al. 2012), and the remaining 20% is due to increases in respiration associated with increased riverine organic carbon input. Specifically, the enhanced flushing pushes the maxima in GPP and respiration downstream by nearly 20 km (Fig. 7d,i), which is consistent with the pattern also found in the mainstem of the Chesapeake Bay in high-flow years (Da et al. 2018). Increased riverine organic carbon delivery increases respiration, especially in the upstream reaches of the YRE (i.e., the Pamunkey River), which is consistent with the enhanced decomposition of riverine organic carbon found in North Carolina estuaries during high discharge conditions (Van Dam et al. 2018).

In coastal plain estuaries, NEP and the carbonate system can exhibit strong variability on shorter time scales as well. For example, NEP is characterized by strong quasi-monthly oscillations in the YRE (Fig. 5a), with the sign of NEP alternating between heterotrophy and autotrophy, even though the system is net heterotrophic on longer time scales. These oscillations are due to interactions between the M_2 and N_2 tidal constituents and result in a quasi-monthly (27.5 days) tidal cycle (e.g., Byun and Hart 2020) in addition to the usual spring-neap cycle. In the YRE where M_2 and N_2 are the largest constituents, this quasi-monthly tidal cycle impacts not only stratification, but also NEP, which together drive quasi-monthly variability in the carbonate system as well. For example, over the 2-week period when conditions transition from strong to weak tides (June 19 to July 4, 2017), the top-to-bottom salinity difference at station LE4.2 (Fig. 1) increases from 3 to 8, vertically integrated GPP increases from 0.8 to 2.7 g-C m^{-2} day^{-1}, and surface DIC decreases from 1394 to 1336 mmol C m^{-3} (Fig. S8). Over the following 2 weeks, the system transitions back to stronger tidal conditions. The stronger tides are associated with increased light limitation, lower phytoplankton production, and higher DIC; in contrast, respiration is comparatively less affected by these tidal modulations. As a result, the system fluctuates between net heterotrophy during strong tides and net autotrophy during weak tides over a quasi-monthly cycle (Fig. 5a). Similar tidal modulations of chlorophyll, oxygen, and pCO_2 are observed in the Hudson River (Scully et al. 2022). This variability should be kept in mind for field campaigns and particularly for water quality monitoring programs, which often sample at approximately monthly intervals.

Estuarine Air-Sea Gas Exchange

Our simulations demonstrate that the YRE is a source of CO_2 to the atmosphere in both the dry and wet years examined. This results from the combination of high DIC/TA ratio in the riverine and wetland inputs and net heterotrophy. Outgassing fluxes for the drier (3.4 mol C m^{-2} $year^{-1}$) and the wetter (4.5 mol C m^{-2} $year^{-1}$) years are slightly lower than the average estuarine CO_2 outgassing rate of 7.7 mol C m^{-2} $year^{-1}$ reported in the global synthesis of Chen et al. (2013). In this respect, the YRE behaves differently than the mainstem Chesapeake Bay, which fluctuates between a weak source and weak sink of CO_2 to the atmosphere, albeit with strong interannual variability (Brodeur et al. 2019; Friedman et al. 2020; Shen et al. 2019; Chen et al. 2020; Herrmann et al. 2020; St-Laurent et al. 2020). For example, Herrmann et al. (2020) found that the Chesapeake Bay outgasses CO_2 at a mean rate of 1.2 mol C m^{-2} $year^{-1}$ over years 1998–2018, with higher CO_2 outgassing under low-flow years, most likely due to decreased net autotrophy associated with low nutrient inputs. In contrast, this study suggests that the YRE is a net source of CO_2 to the atmosphere regardless of the flow conditions. In fact, a sensitivity simulation where biological sinks and sources of DIC and TA were deactivated

reveals that air-sea CO_2 exchange is similar under contrasting flow conditions (i.e., 2.6 and 2.4 mol C m^{-2} $year^{-1}$ in the drier and wetter year, respectively; Fig. S9). This suggests that the year-to-year variability in air-sea CO_2 flux is primarily driven by the changes in NEP, whereas the outgassing nature of the YRE is fundamentally driven by high riverine and wetland DIC/TA ratio. In addition, including tidal wetlands in the model more than doubles CO_2 outgassing (increase of 137%) because of the combination of increased net heterotrophy and increased wetland DIC/TA ratio (Figs. 3 and 4). This result is supported by the work of Wang et al. (2016) who showed that tidal water has higher degassing potential after exchange with marshes due to added DIC and TA via aerobic and anaerobic respiration. The recent global synthesis by Reithmaier et al. (2023) also shows that saltmarsh sediments generally produce more DIC than TA, potentially contributing to more CO_2 outgassing in surface waters. Our results may actually underestimate the impact of tidal wetlands, as the annual mean tidal wetland DIC inputs used in this study are 4.0 and 5.1 mol C m^{-2} $year^{-1}$ for the 2 years examined (per unit area of tidal wetlands), which are considerably lower than the values for Eastern North America (Najjar et al. 2018; 19.6 ± 10 mol C m^{-2} $year^{-1}$) and the Sweet Hall Marsh in the YRE (Neubauer and Anderson 2003; 16.4 mol C m^{-2} $year^{-1}$). However, it is possible that the value from Neubauer and Anderson (2003) is biased high, as it was calculated from data over ebb tides only.

The air-sea CO_2 exchange rate in this study can be compared to estimates from previous studies in the same region. Previous observations by Bukaveckas (2022) from 2017 to 2019 suggest that the annual mean CO_2 outgassing rate in the Pamunkey tributary is 90 mol C m^{-2} $year^{-1}$. This estimate is much higher than the mean rate calculated for the Pamunkey by Raymond et al. (2000) in 1997 (21 mol C m^{-2} $year^{-1}$) and in this study (13 mol C m^{-2} $year^{-1}$); however, annual average pCO_2 levels are similar in all these studies (~2000 µatm). The difference in CO_2 outgassing could be due to the choice of gas transfer velocity. This study uses the gas transfer velocity that is a function of wind speed (Wanninkhof 2014) as in previous Chesapeake Bay studies (Raymond et al. 2000; Shadwick et al. 2019; Chen et al. 2020; Herrmann et al. 2020; Da et al. 2021), whereas Bukaveckas (2022) used a higher and constant gas transfer velocity appropriate for river systems where current velocity may play an important role (Raymond et al. 2017). Although the majority of the YRE behaves more like an estuarine system with open water, where wind primarily drives gas transfer velocity, the choice of gas transfer velocity in its small tributaries and headwaters would benefit from future investigation. Nevertheless, there is agreement among all these studies that the rate of CO_2 outgassing is higher in the summer in the YRE (Fig. 7b, g), which is likely driven by increased temperatures and higher tidal wetland inputs of DIC (Fig. 5b; Wang et al. 2016; Yao et al. 2022). The lower YRE, however, could be a sink for atmospheric CO_2 during the winter and spring when biological uptake of CO_2 is high (Shadwick et al. 2019). Our results show periodic net uptake of atmospheric CO_2 in the lower YRE at this time of year (Fig. 7b, g), depending on the phase of the quasi-monthly tidal cycle. For example, surface pCO_2 at LE4.2 (Fig. 1) decreases from 760 to 240 µatm over the 2-week period of June 19 to July 4, 2017 due to weakened tides and enhanced GPP at the surface (Fig. S8).

Sources and Sinks of TA

Biological processes act as a sink of TA in the estuarine water column and a source of TA in estuarine sediments. Our model results suggest net estuarine TA production of 0.92 mmol m^{-2} day^{-1} (drier year) and 0.48 mmol m^{-2} day^{-1} (wetter year), which results from a complex combination of sources and sinks related to nitrogen and sulfur cycling in the water column and sediment. When taking nitrogen cycling in the water column together, phytoplankton uptake of NH_4^+ and NO_3^- and release of NH_4^+ from aerobic respiration, nitrification, and denitrification are overall a sink of TA, with annual mean rates of -0.11 mmol m^{-2} day^{-1} (drier year) and -0.49 mmol m^{-2} day^{-1} (wetter year). The greater TA sink via the nitrogen cycle in the wetter year is primarily driven by increased nitrification in the water column (Table 2). Net sulfate reduction occurring in the sediment is the primary source of TA and is characterized by similar annual mean rates in both years (~1.0 mmol m^{-2} day^{-1}). This rate depends on our model's assumption that one-third of the produced sulfite is permanently buried (Roden and Tuttle 1993). Increasing the sulfide burial fraction to one-half would cause this rate to slightly increase to ~1.2 mmol m^{-2} day^{-1}. Only a small portion of TA production in sediment (< 5%) is due to NH_4^+ production via aerobic respiration and coupled net nitrification–denitrification. Based on mass balance approximations, previous estimates of internal TA production in the Pamunkey-York River are 8 mmol m^{-2} day^{-1} (Raymond et al. 2000) and 12 ± 5 mmol m^{-2} day^{-1} ($\pm$ 1 standard error; Najjar et al. 2020), and the estimate in the Mattaponi-York River is 15 ± 5 mmol m^{-2} day^{-1}(Najjar et al. 2020). These mass balance approximations were calculated for the whole estuarine system, including tidal wetlands, water column, and sediments. To make a comparison between our model results and these prior estimates, we must include the source of alkalinity from tidal wetlands, which amounts to 1.3 and 2.6 mmol m^{-2} day^{-1} in the drier and the wetter years, respectively, leading to total TA production of 2.2 and 3.1 mmol m^{-2} day^{-1}. Even after including these wetland sources, our model-based estimates of internal sources of TA are considerably lower than estimates based on the mass

balance approximations. It is possible that there are other important biogeochemical sources of TA that are missing from the current model implementation. For example, the inclusion of calcium carbonate dissolution (Su et al. 2020) and iron and manganese reduction in estuarine sediments (Thibault de Chanvalon et al. 2022), in combination with a more comprehensive sediment diagenesis module (e.g., Radtke et al. 2019), would likely more accurately simulate TA production in the sediments. However, estimates of estuarine TA sources are very limited and typically indirectly based on the distributions of carbonate system variables and steady-state mixing-model assumptions (e.g., Raymond et al. 2000; Najjar et al. 2020). Field measurements of Ca^{2+}, sulfate, iron, manganese, and TA fluxes would be necessary to more robustly quantify and determine the processes underlying biological sources and sinks of TA in the YRE and other coastal plain estuaries.

Estuarine TA sources and sinks are strongly influenced by both quasi-monthly tidal cycles and high discharge events. Because phytoplankton uptake of NH_4^+ and NO_3^- has opposite influences on TA (Wolf-Gladrow et al. 2007) and each uptake process is strongly influenced by tidal cycles, the net impact on TA from phytoplankton production shows little quasi-monthly variability (Fig. 6a). Although the source of TA via total respiration has a weak relationship with tidal energy, net sulfate reduction in the sediments exhibits a strong negative relationship with tides because less organic matter reaches the seafloor for anaerobic respiration when tides are stronger. In contrast, nitrification impacts on TA are positively related to the quasi-monthly tidal cycle, with stronger TA consumption via nitrification during stronger tides when biological uptake of NH_4^+ is lower and more NH_4^+ is available for oxidation to NO_3^-. Additionally, strong flushing inhibits GPP (e.g., Paerl and Huisman 2008; Lucas et al. 2009; Peierls et al. 2012) and decreases biological uptake of NH_4^+, which increases nitrification during high river discharge events (e.g., May 2018; Fig. 6a) and counters the enhanced TA production associated with increased respiration. This is evident and even results in consistent TA sinks via total biological processes when river discharge is consistently high from October to December 2018 (Fig. 6a). Because of the short-term variability in various TA sources and sinks, it is important to consider tidal variability and flow conditions when designing sulfate, nitrogen, and TA field experiments.

TA input from tidal wetlands is a crucial component of the TA budget. Although DIC inputs from tidal wetlands have been estimated for many coastal regions (Chu et al. 2018; Najjar et al. 2018; Alongi 2020; Bogard et al. 2020; Tamborski et al. 2021; Yao et al. 2022), TA exchanges between wetlands and coastal waters are rarely measured directly (Wang et al. 2016; Yau et al. 2022) and typically are not accounted for in coupled hydrodynamic-biogeochemical models. In this study, lateral transport of TA from tidal wetlands accounts for roughly 25% of the riverine input, suggesting that wetland inputs of TA play an important role in carbon sequestration (Wang and Cai 2004; Hu and Cai 2011; Santos et al. 2021). Including tidal wetland TA inputs in the model impacts DIC speciation, with the additional inputs of DIC being stored in the estuary as carbonate alkalinity, instead of mostly being outgassed to the atmosphere. The annual mean rate of TA inputs from tidal wetlands is 3 mmol m^{-2} day^{-1} (drier year) and 6 mmol m^{-2} day^{-1} (wetter year), where these model fluxes are now provided per unit area of tidal wetlands. These lateral fluxes of TA are lower than those measured from salt marshes in the east coast of China (78 ± 75 mmol m^{-2} day^{-1}; Yau et al. 2022) and those measured from mangrove/salt marsh creeks along the east coast of Australia (12 ± 6 mmol m^{-2} day^{-1}; Santos et al. 2019); however, the spatiotemporal variability in these estimates is high. To determine whether sources of TA to the YRE are accurately represented in this study, additional TA flux measurements in tidal wetlands are needed, with care taken to properly sample wetlands across different redox-sensitive elements, and in different salinity regimes since the sources of TA may vary with salinity. For example, sulfate reduction is likely a more important source of TA in saline marshes (Hu and Cai 2011) than in fresh marshes. Losses of NO_3^- and NH_4^+ in marsh sediment via vegetation uptake and denitrification could impact TA levels in adjacent estuarine waters (Williams et al. 2006; Cai et al. 2023). Previous model simulations indicate that decreases in NO_3^- and NH_4^+ concentrations due to tidal marshes are less than 5 mmol N m^{-3} in the YRE (Cai et al. 2023), suggesting that the resulting impact on TA concentrations via nitrogen cycle could be minimal. However, as pointed out in previous studies, systematic measurements are needed to further improve the model and better understand the nitrogen cycle and its interaction with tidal marshes.

Lateral Exchange of DIC and TA with the Chesapeake Bay

Previous studies generally have classified estuaries as net sources of inorganic carbon to the continental shelf and coastal regions (Cai et al. 2003; Chen and Borges 2009; Najjar et al. 2018). This is also true for the Chesapeake Bay (Brodeur et al. 2019; St-Laurent et al. 2020) as well as for the tidal fresh region of the Potomac River Estuary (Cerco et al. 2013), which is the second largest tributary of the Chesapeake Bay. Similarly, our study suggests that the YRE exports DIC and TA to the mainstem of the Bay on annual time scales, although these rates exhibit large year-to-year variability (Fig. 3). The substantially greater exports

of DIC and TA to the Bay in 2018 are partially driven by the increased river inputs to the YRE. Additionally, in this wetter year, increased discharge in the larger Chesapeake Bay tributaries (e.g., the Susquehanna and the Potomac Rivers) dilutes DIC and TA concentrations in the mainstem Chesapeake Bay outside of the YRE mouth, which reduces bottom influx of DIC and TA into the YRE. Together, the additive effects of increased surface outflux and decreased bottom influx of DIC and TA at the mouth of the YRE result in substantially greater exports to the Chesapeake Bay in the wetter year (2018) compared to the drier year (2017). Additionally, the dilution effects from both the excess river water and the diluted Bay water entering the YRE contribute to the low TA and DIC concentrations in 2018. Significant seasonal variability exists as well, as the system receives DIC from the lower Chesapeake Bay in the summer to compensate for DIC losses due to outgassing and biological uptake of CO_2 (Fig. 5).

Summary and Concluding Remarks

A 3D estuarine hydrodynamic-biogeochemistry model with empirical inputs from tidal wetlands is used to investigate advective and biogeochemical sources and sinks of DIC and TA in the YRE. River inputs, tidal wetlands, and quasi-monthly tidal cycles each significantly impacts the carbonate system in this coastal plain estuary, and the relative contributions of these drivers are shown to vary over different temporal and spatial scales:

- Year-to-year variability of the carbonate system is primarily driven by changing river inputs. Compared to the year examined with average flow conditions, net DIC production due to biological processes (i.e., net heterotrophy) is three times higher in the wetter year, with decreased phytoplankton growth due to increased flushing and light limitation playing the dominant role. This enhanced net heterotrophy also drives greater CO_2 outgassing to the atmosphere. Spatial maxima of biological DIC and TA sources and sinks are pushed downstream by nearly 20 km due to increased flushing. The exports of DIC and TA to the mainstem Chesapeake Bay are also three to four times greater under high flow conditions.
- Quasi-monthly variability in biological controls of the carbonate system is driven by the tides. Specifically, stronger tides increase mixing and decrease vertical stratification. This lowers phytoplankton growth by increasing light limitation, leading to more net DIC production. Biological sources and sinks of TA, such as nitrification and net sulfate reduction, additionally exhibit quasi-monthly tidal variability.
- Tidal wetlands have a notable impact on the carbonate system with wetlands accounting for 20–30% of the total DIC and TA sources to the YRE. Including the impacts of wetlands in the model increases estuarine CO_2 outgassing by a factor of 2 and partially contributes to net heterotrophy over annual time scales. In other estuaries where the ratio of tidal wetland area to the total surface area of the estuary is lower, tidal wetlands may not have as large an impact on the carbonate system.

Overall, this study highlights that carbonate chemistry in tidal tributaries experience complex transformations due to a combination of influences from the watershed, tidal wetlands, and ocean. New observational data in concert with state-of-the-art coupled hydrodynamic-biogeochemical models allow a better understanding of these complex ecosystems; however, additional observations are specifically required to (1) better constrain lateral fluxes of DIC and TA between tidal wetlands and estuarine waters, and (2) quantify the role of coastal vegetation on global carbon and alkalinity cycling. Ultimately such data will help improve the parameterizations included in coastal biogeochemical models such as the one used in this study.

Smaller estuaries such as the YRE are important sites for shellfish aquaculture (Beckensteiner et al. 2020, 2021; Reece et al. 2020) and oyster habitat restoration (Bersoza Hernández et al. 2018; Ridlon et al. 2021; Carey 2021); however, these systems are especially vulnerable to dynamic pH and calcium carbonate saturation state conditions which can be strongly impacted by changing climate and local runoff (Waldbusser et al. 2011; Siedlecki et al. 2017; Doney et al. 2020; Da et al. 2021; Vargas et al. 2022). This study showed that high freshwater discharge events substantially impact sources and sinks of DIC and TA, which will have considerable impacts on calcium carbonate saturation states as well. With the projected future increases in precipitation intensity projected for the Chesapeake Bay (St. Laurent et al. 2021; Hinson et al. 2023), tidal tributaries will likely experience even more rapid changes in carbonate chemistry in the future. Such changes may detrimentally stress economically and ecologically important calcifying species in the region. Additional studies investigating tidal wetlands and their responses to extreme events may help us better understand how the estuarine carbonate system will change in the future, and how economically and ecologically important calcifying organisms will be impacted as a result.

Supplementary Information The online version contains supplementary material available at https://doi.org/10.1007/s12237-024-01421-z.

Acknowledgements The authors thank Maria Herrmann and Rusty Feagin for providing instructions on processing wetland GPP data, as well as Scott Doney. Emily Rivest, and Carl Friedrichs for their advice

throughout the project. Many thanks to the Chesapeake Bay Program Watershed Modeling team for providing riverine model inputs from the watershed. This work is conducted using William & Mary's High Performance Computing facilities, which are supported by the National Science Foundation, the Commonwealth of Virginia Equipment Trust Fund and the Office of Naval Research.

Author Contribution All authors contributed to the study conception, methodology, and investigation. Data curation, analysis, and visualization were performed by Fei Da. The first draft of the manuscript was written by Fei Da, and all authors provided comments and edits on previous versions. All authors read and approved the final manuscript.

Funding This paper is the result of research funded by the National Oceanic and Atmospheric Administration's Ocean Acidification Program (NOAA OAP) under award NA20OAR0170473 to VIMS. Additional funding has been provided by the Mid-Atlantic Sea Grant/NOAA OAP Graduate Research Fellowship (NA14OAR4170093, NA18OAR4170083), the National Science Foundation (OCE-2148952 and OCE-2148949), the Virginia Institute of Marine Science Foundation, and the United States Geological Survey Climate Research & Development Program.

Data Availability ROMS-ECB model code, input files, and model outputs are permanently archived at the W&M ScholarWorks data repository associated with this article and are available for free download, https://doi.org/10.25773/2yme-ry62.

Declarations

Conflict of Interest The authors declare no competing interests.

References

Alongi, D.M. 2020. Carbon balance in salt marsh and mangrove ecosystems: A global synthesis. *Journal of Marine Science and Engineering* 8 (10): 767. https://doi.org/10.3390/jmse8100767.

Anderson, G.F. 1986. Silica, diatoms and a freshwater productivity maximum in Atlantic Coastal Plain estuaries, Chesapeake Bay. *Estuarine, Coastal and Shelf Science* 22 (2): 183–197. https://doi.org/10.1016/0272-7714(86)90112-5.

Bhatt, G., L. Linker, G. Shenk, I. Bertani, et al. 2023. Water quality impacts of climate change, land use, and population growth in the Chesapeake Bay watershed. *Journal of the American Water Resources Association*, 1–29. https://doi.org/10.1111/1752-1688.13144.

Beckensteiner, J., D.M. Kaplan, and A.M. Scheld. 2020. Barriers to Eastern Oyster Aquaculture Expansion in Virginia. *Frontiers in Marine Science* 7: 53. https://doi.org/10.3389/fmars.2020.00053.

Beckensteiner, J., A.M. Scheld, P. St-Laurent, M.A.M. Friedrichs, and D.M. Kaplan. 2021. Environmentally-determined production frontiers and lease utilization in Virginia's eastern oyster aquaculture industry. *Aquaculture* 542: 736883. https://doi.org/10.1016/j.aquaculture.2021.736883.

Bersoza Hernández, A., R.D. Brumbaugh, P. Frederick, R. Grizzle, M.W. Luckenbach, C.H. Peterson, and C. Angelini. 2018. Restoring the eastern oyster: How much progress has been made in 53 years? *Frontiers in Ecology and the Environment* 16 (8): 463–471. https://doi.org/10.1002/fee.1935.

Brodeur J.R., B. Chen, J. Su, Y. Xu, N. Hussain, K.M. Scaboo, Y. Zhang, J.M. Testa, and W.-J. Cai. 2019. Chesapeake bay inorganic carbon: spatial distribution and seasonal variability. *Frontier in Marine Science* 6 (99). https://doi.org/10.3389/fmars.2019.00099.

Bogard, M.J., B.A. Bergamaschi, D.E. Butman, F. Anderson, S.H. Knox, and L. Windham-Myers. 2020. Hydrologic export is a major component of coastal wetland carbon budgets. *Global Biogeochemical Cycles* 34: e2019GB006430. https://doi.org/10.1029/2019GB006430.

Bukaveckas, P.A., L.E. Barry, M.J. Beckwith, V. David, and B. Lederer. 2011. Factors determining the location of the chlorophyll maximum and the fate of algal production within the tidal freshwater James River. *Estuaries and Coasts* 34: 569–582. https://doi.org/10.1007/s12237-010-9372-4.

Bukaveckas, P.A., S. Tassone, W.M. Lee, and R.B. Franklin. 2020. The influence of storm events on metabolism and water quality of riverine and estuarine segments of the James, Mattaponi and Pamunkey Rivers. *Estuaries and Coasts* 43: 1585–1602. https://doi.org/10.1007/s12237-020-00819-9.

Bukaveckas, P.A. 2022. Carbon dynamics at the river–estuarine transition: a comparison among tributaries of Chesapeake Bay. *Biogeosciences* 19: 4209–4226. https://doi.org/10.5194/bg-19-4209-2022.

Byun, D.-S., and D.E. Hart. 2020. A monthly tidal envelope classification for semidiurnal regimes in terms of the relative proportions of the S_2, N_2, and M_2 constituents. *Ocean Science* 16: 965–977. https://doi.org/10.5194/os-16-965-2020.

Cai, W.-J., and Y. Wang. 1998. The chemistry, fluxes, and sources of carbon dioxide in the estuarine waters of the Satilla and Altamaha Rivers, Georgia. *Limnology and Oceanography* 43 (4): 657–668. https://doi.org/10.4319/lo.1998.43.4.0657.

Cai, W.-J., Z.A. Wang, and Y. Wang. 2003. The role of marsh-dominated heterotrophic continental margins in transport of CO_2 between the atmosphere, the land-sea interface and the ocean. *Geophysical Research Letters* 30 (16): 1849. https://doi.org/10.1029/2003GL017633.

Cai, W.-J., X. Hu, W. Huang, M.C. Murrell, et al. 2011. Acidification of subsurface coastal waters enhanced by eutrophication. *Nature Geoscience* 4 (11): 766–770. https://doi.org/10.1038/ngeo1297.

Cai, W.-J., W. Huang, G.W. Luther, D. Pierrot, et al. 2017. Redox reactions and weak buffering capacity lead to acidification in the Chesapeake Bay. *Nature Communications* 8: 369. https://doi.org/10.1038/s41467-017-00417-7.

Cai, W.-J., R.A. Feely, J.M. Testa, M. Li, et al. 2020. Natural and anthropogenic drivers of acidification in large estuaries. *Annual Review of Marine Science* 13: 1. https://doi.org/10.1146/annurev-marine-010419-011004.

Cai, X., J. Shen, Y.J. Zhang, Q. Qin, and L. Linker. 2023. The roles of tidal marshes in the estuarine biochemical processes: A numerical modeling study. *Journal of Geophysical Research:*

Biogeosciences 128: e2022JG007066. https://doi.org/10.1029/2022JG007066.

Canuel, E.A., and A.K. Hardison. 2016. Sources, ages, and alteration of organic matter in estuaries. *Annual Review of Marine Science* 8 (1): 409–434. https://doi.org/10.1146/annurev-marine-122414-034058.

Carey, J. 2021. News feature: The complex case of Chesapeake Bay restoration. *Proceedings of the National Academy of Sciences* 118: e2108734118. https://doi.org/10.1073/pnas.2108734118.

Cerco, C.F., T. Threadgill, M.R. Noel, and S. Hinz. 2013. Modeling the pH in the tidal fresh Potomac River under conditions of varying hydrology and loads. *Ecological Modelling* 257: 101–112. https://doi.org/10.1016/j.ecolmodel.2013.02.011.

Chen, C.-T.A., and A.V. Borges. 2009. Reconciling opposing views on carbon cycling in the coastal ocean: continental shelves as sinks and near-shore ecosystems as sources of atmospheric CO_2. *Deep Sea Research Part II* 33: L12603. https://doi.org/10.1016/j.dsr2.2009.01.001.

Chen, C.-T.A., T.-H. Huang, Y.-C. Chen, Y. Bai, X. He, and Y. Kang. 2013. Air-sea exchanges of CO_2 in the world's coastal seas. *Biogeosciences* 10: 6509–6544. https://doi.org/10.5194/bg-10-6509-2013.

Chen, B., W.-J. Cai, J.R. Brodeur, N. Hussain, J.M. Testa, W. Ni, and Q. Li. 2020. Seasonal and spatial variability in surface pCO_2 and air–water CO_2 flux in the Chesapeake Bay. *Limnology and Oceanography* 65: 3046–3065. https://doi.org/10.1002/lno.11573.

Chesapeake Bay National Estuarine Research Reserve in Virginia, Virginia Institute of Marine Science (CBNERR-VA VIMS). 2022. Virginia Estuarine and Coastal Observing System (VECOS). Data accessed from VECOS website: http://vecos.vims.edu. accessed in May 2022.

Chesapeake Bay Program (CBP). 2022. Chesapeake Bay program water quality monitoring data. Data accessed from CBP website: https://www.chesapeakebay.net/what/downloads/cbp-water-quality-database-1984-present. Accessed May 2022.

Chu, S.N., Z.A. Wang, M.E. Gonneea, K.D. Kroeger, and N.K. Ganju. 2018. Deciphering the dynamics of inorganic carbon export from intertidal salt marshes using high-frequency measurements. *Marine Chemistry* 206: 7–18. https://doi.org/10.1016/j.marchem.2018.08.005.

Clark, J.B., W. Long, and R.R. Hood. 2020. A comprehensive estuarine dissolved organic carbon budget using an enhanced biogeochemical model. *Journal of Geophysical Research: Biogeosciences* 125: e2019JG005442. https://doi.org/10.1029/2019JG005442.

Cronin, W.B. 1971. Volumetric, areal, and tidal statistics of the Chesapeake Bay estuary and its tributaries. Chesapeake Bay Institute, Special Report 20. Washington, D.C.: Johns Hopkins University, p 135.

Da, F., M.A.M. Friedrichs, and P. St-Laurent. 2018. Impacts of atmospheric nitrogen deposition and coastal nitrogen fluxes on Chesapeake Bay hypoxia. *Journal of Geophysical Research: Oceans* 123 (7): 5004–5025. https://doi.org/10.1029/2018JC014009.

Da, F., M.A.M. Friedrichs, P. St-Laurent, E.H. Shadwick, R.G. Najjar, and K.E. Hinson. 2021. Mechanisms driving decadal changes in the carbonate system of a coastal plain estuary. *Journal of Geophysical Research: Oceans* 126: e2021JC017239. https://doi.org/10.1029/2021JC017239.

Dai, M., J. Su, Y. Zhao, E.E. Hofmann, et al. 2022. Carbon fluxes in the Coastal Ocean: Synthesis, boundary processes, and future trends. *Annual Review of Earth and Planetary Sciences* 50 (1): 593–626. https://doi.org/10.1146/annurev-earth-032320-090746.

Dinauer, A., and A. Mucci. 2017. Spatial variability in surface-water pCO2 and gas exchange in the world's largest semi-enclosed estuarine system: St. Lawrence estuary (Canada). *Biogeosciences* 14 (13): 3221–3237. https://doi.org/10.5194/bg-14-3221-2017.

Doney, S.C., D.S. Busch, S.R. Cooley, and K.J. Kroeker. 2020. The impacts of ocean acidification on marine ecosystems and reliant human communities. *Annual Review of Environment and Resources* 45: 83–112. https://doi.org/10.1146/annurev-environ-012320-083019.

Ekstrom, J.A., L. Suatoni, S.R. Cooley, L.H. Pendleton, et al. 2015. Vulnerability and adaptation of US shellfisheries to ocean acidification. *Nature Climate Change* 5: 207–214. https://doi.org/10.1038/nclimate2508.

Feagin, R.A., I. Forbrich, T.P. Huff, J.G. Barr, J. Ruiz-Plancarte, et al. 2020. Tidal wetland gross primary production across the continental United States, 2000–2019. *Global Biogeochemical Cycles* 34: e2019GB006349. https://doi.org/10.1029/2019GB006349.

Feely, R.A., S.R. Alin, J. Newton, C.L. Sabine, M. Warner, A. Devol, C. Krembs, and C. Maloy. 2010. The combined effects of ocean acidification, mixing, and respiration on pH and carbonate saturation in an urbanized estuary. *Estuarine, Coastal and Shelf Science* 88 (4): 442–449. https://doi.org/10.1016/j.ecss.2010.05.004.

Feng, Y., M.A.M. Friedrichs, J. Wilkin, H. Tian, Q. Yang, E.E. Hofmann, J.D. Wiggert, and R.R. Hood. 2015. Chesapeake Bay nitrogen fluxes derived from a land-estuarine ocean biogeochemical modeling system: Model description, evaluation, and nitrogen budgets. *Journal of Geophysical Research: Biogeosciences* 120 (8): 1666–1695. https://doi.org/10.1002/2015JG002931.

Fennel, K., J. Wilkin, J. Levin, J. Moisan, J. O'Reilly, and D. Haidvogel. 2006. Nitrogen cycling in the Mid Atlantic Bight and implications for the North Atlantic nitrogen budget: results from a three-dimensional model. *Global Biogeochemical Cycles* 20: GB3007. https://doi.org/10.1029/2005GB002456.

Friedman, J.R., E.H. Shadwick, M.A.M. Friedrichs, R.G. Najjar, O.A. DeMeo, F. Da, and J. Smith. 2020. Seasonal variability of the CO_2 system in a large coastal plain estuary. *Journal of Geophysical Research: Oceans* 125 (1). https://doi.org/10.1029/2019JC015609.

Friedrichs, C.T. 1995. Stability shear stress and equilibrium cross-sectional geometry of sheltered tidal channels. *Journal of Coastal Research* 11: 1062-1074. https://www.jstor.org/stable/4298411

Friedrichs, C.T. 2009. York River physical oceanography and sediment transport. *Journal of Coastal Research* 10057: 17–22. https://doi.org/10.2112/1551-5036-57.sp1.17.

Haas, L.W. 1977. The effect of the spring-neap tidal cycle on the vertical salinity structure of the James, York, and Rappahannock Rivers, Virginia, U.S.A. *Estuarine and Coastal Marine Science* 5: 485–496.

Henderson, R., and P.A. Bukaveckas. 2022. Factors governing light attenuation in upper segments of the James and York Estuaries and their influence on primary producers. *Estuaries and Coasts* 45: 470–484. https://doi.org/10.1007/s12237-021-00983-6.

Herrmann, M., R.G. Najjar, W.M. Kemp, R.B. Alexander, E.W. Boyer, W.-J. Cai, P.C. Griffith, K.D. Kroeger, S.L. McCallister, and R.A. Smith. 2015. Net ecosystem production and organic carbon balance of U.S. East Coast Estuaries: a synthesis approach. *Global Biogeochemical Cycles* 29: 96–111. https://doi.org/10.1002/2013GB004736.

Herrmann, M., R.G. Najjar, F. Da, J.R. Friedman, M.A.M. Friedrichs, S. Goldberger, A. Menendez, E.H. Shadwick, E.G. Stets, and P. St-Laurent. 2020. Challenges in quantifying air-water carbon dioxide flux using estuarine water quality data: Case study for Chesapeake Bay. *Journal of Geophysical Research: Oceans* 125: e2019JC015610. https://doi.org/10.1029/2019JC015610.

Hersbach, H., B. Bell, P. Berrisford, G. Biavati, A. Horányi, J. Muñoz Sabater, J. Nicolas, C. Peubey, R. Radu, I. Rozum, D. Schepers, A. Simmons, C. Soci, D. Dee, and J-N. Thépaut. 2023. ERA5 hourly data on single levels from 1940 to present . Copernicus

Climate Change Service (C3S) Climate Data Store (CDS). https://doi.org/10.24381/cds.adbb2d47.

Hinson, K.E., M.A.M. Friedrichs, R.G. Najjar, M. Herrmann, Z. Bian, G. Bhatt, P. St-Laurent, H. Tian, and G. Shenk. 2023. Impacts and uncertainties of climate-induced changes in watershed inputs on estuarine hypoxia. *Biogeosciences* 20: 1937–1961. https://doi.org/10.5194/bg-20-1937-2023.

Hirsch, R.M., D.L. Moyer, and S.A. Archfield. 2010. Weighted regressions on time, discharge, and season (WRTDS), with an application to Chesapeake Bay river inputs. *Journal of the American Water Resources Association* 46 (5): 857–880. https://doi.org/10.1111/j.1752-1688.2010.00482.x.

Hirsch, R.M., and L.A. De Cicco. 2015. User guide to Exploration and Graphics for RivEr Trends (EGRET) and dataRetrieval—R packages for hydrologic data (version 1.0: Originally posted October 8, 2014; version 2.0: February 5, 2015). U.S. Geological Survey Techniques and Methods, 4-A10. https://doi.org/10.3133/tm4A10.

Hopkinson, C.S., I. Buffam, J. Hobbie, and J. Vallino. 1998. Terrestrial inputs of organic matter to coastal ecosystems: An intercomparison of chemical characteristics and bioavailability. *Biogeochemistry* 43: 211–234. https://doi.org/10.1023/A:1006016030299.

Hornberger, G.M., M.G. Kelly, and B.J. Cosby. 1977. Evaluating eutrophication potential from river community productivity. *Water Research* 11: 65–69. https://doi.org/10.1016/0043-1354(77)90183-X.

Hu, X., and W.-J. Cai. 2011. An assessment of ocean margin anaerobic processes on oceanic alkalinity budget. *Global Biogeochemical Cycles* 25: GB3003. https://doi.org/10.1029/2010GB003859.

Hu, X., H. Yao, C.J. Staryk, M.R. McCutcheon, M.S. Wetz, and L. Walker. 2020. Disparate responses of carbonate system in two adjacent subtropical estuaries to the influence of Hurricane Harvey – A case study. *Frontiers in Marine Science* 7: 26. https://doi.org/10.3389/fmars.2020.00026.

Jolliff, J.K., J.C. Kindle, I. Shulman, B. Penta, M.A.M. Friedrichs, R. Helber, and R.A. Arnone. 2009. Summary diagrams for coupled hydrodynamic-ecosystem model skill assessment. *Journal of Marine Systems* 76 (1–2): 64–82. https://doi.org/10.1016/j.jmarsys.2008.05.014.

Jørgensen, B.B. 1996. *Material flux in the sediment. Eutrophication in Coastal Marine Ecosystems*. vol. 52, edited by B.B. Jørgensen and K. Richardson, 115-135. Washington, D.C.: American Geophysical Union. https://doi.org/10.1029/CE052p0115.

Kaushal, S.S., G.E. Likens, R.M. Utz, M.L. Pace, M. Grese, and M. Yepsen. 2013. Increased river alkalinization in the Eastern U.S. *Environmental Science & Technology* 47 (18): 10302–10311. https://doi.org/10.1021/es401046s.

Kemp, W.M., E.M. Smith, M. Marvin-DiPasquale, and W.R. Boynton. 1997. Organic carbon balance and net ecosystem metabolism in Chesapeake Bay. *Marine Ecology Progress Series* 150: 229–248. https://doi.org/10.3354/meps150229.

Kemp, W.M., and J.M. Testa. 2011. Metabolic balance between ecosystem production and consumption. In *Treatise on Estuarine and Coastal Science*, vol. 5, ed. E. Wolansky and D. McLusky, 83–118. Oxford, U. K.: Academic Press.

Kim, J., M.J. Brush, B. Song, and I.C. Anderson. 2021. Reconstructing primary production in a changing estuary: A mass balance modeling approach. *Limnology and Oceanography* 66: 2535–2546. https://doi.org/10.1002/lno.11771.

Knobloch, A.L.J., W.G. Reay, and E.A. Canuel. 2021. Carbon pools differ in source and temporal patterns in a tidal marsh creek system of the York River, VA Estuary. *Estuaries and Coasts* 44: 1848–1865. https://doi.org/10.1007/s12237-020-00878-y.

Lacroix, F., T. Ilyina, G.G. Laruelle, and P. Regnier. 2021. Reconstructing the preindustrial coastal carbon cycle through a global ocean circulation model: Was the global continental shelf already both autotrophic and a CO_2 sink? *Global Biogeochemical Cycles* 35: e2020GB006603.

Lake, S.J., and M.J. Brush. 2015. Contribution of nutrient and organic matter sources to the development of periodic hypoxia in a tributary estuary. *Estuaries and Coasts* 38: 2149–2171.

Lucas, L.V., J.K. Thompson, and L.R. Brown. 2009. Why are diverse relationships observed between phytoplankton biomass and transport time? *Limnology and Oceanography* 54. https://doi.org/10.4319/lo.2009.54.1.0381.

Mackin, J.E., and K.T. Swider. 1989. Organic matter decomposition pathways and oxygen consumption in coastal marine sediments. *Journal of Marine Research* 47: 681–716. https://doi.org/10.1357/002224089785076154.

Marvin-DiPasquale, M.C., and D.G. Capone. 1998. Benthic sulfate reduction along the Chesapeake Bay central channel. I. Spatial trends and controls. *Marine Ecology Progress Series* 168: 213–228. https://doi.org/10.3354/meps168213.

Mitchell, M., J. Herman, D.M. Bilkovic, and C. Hershner. 2017. Marsh persistence under sea-level rise is controlled by multiple, geologically variable stressors. *Ecosystem Health and Sustainability* 3 (10): 1379888.

Moore, K.A. 2009. Submerged aquatic vegetation of the York River. *Journal of Coastal Research* 10057: 50–58. https://doi.org/10.2112/1551-5036-57.sp1.50.

Moran, M.A., and R.E. Hodson. 1989. Formation and bacterial utilization of dissolved organic carbon derived from detrital lignocellulose. *Limnology and Oceanography* 34. https://doi.org/10.4319/lo.1989.34.6.1034

Mulholland, M.R., R. Morse, T. Egerton, P.W. Bernhardt, and K.C. Filippino. 2018. Blooms of dinoflagellate mixotrophs in a lower Chesapeake Bay tributary: carbon and nitrogen uptake over diurnal, seasonal, and interannual timescales. *Estuaries and Coasts* 41: 1744–1765.

Najjar, R.G., M. Herrmann, R. Alexander, E.W. Boyer, et al. 2018. Carbon budget of tidal wetlands, estuaries, and shelf waters of eastern North America. *Global Biogeochemical Cycles* 32: 389–416. https://doi.org/10.1002/2017GB005790.

Najjar, R.G., M. Herrmann, S. Cintron Del Valle, J.R. Friedman, M.A.M. Friedrichs, L.A. Harris, E.H. Shadwick, E.G. Stets, and R.J. Woodland. 2020. Alkalinity in tidal tributaries of the Chesapeake Bay. *Journal of Geophysical Research: Oceans* 125: e2019JC015597. https://doi.org/10.1029/2019JC015597.

National Oceanic and Atmospheric Administration National Centers for Environmental Information (NOAA NCEI). 2019. Monthly National Climate Report for Annual 2018. https://www.ncei.noaa.gov/access/monitoring/monthly-report/national/201813. Accessed 15 August 2022.

National Oceanic and Atmospheric Administration Tides and Currents. n.d.. https://tidesandcurrents.noaa.gov/stationhome.html?id=8637689. Accessed 20 Dec 2022.

Neubauer, S.C., and I.C. Anderson. 2003. Transport of dissolved inorganic carbon from a tidal freshwater marsh to the York River estuary. *Limnology and Oceanography* 1. https://doi.org/10.4319/lo.2003.48.1.0299.

Neubauer, S.C., I.C. Anderson, and B.B. Neikirk. 2005. Nitrogen cycling and ecosystem exchanges in a Virginia tidal freshwater marsh. *Estuaries* 28: 909–922. https://doi.org/10.1007/BF02696019.

Nichols, M.M., S.C. Kim, and C.M. Brouwer. 1991. Sediment characterization of Chesaapeake Bay and its tributaries. Virginia Institute of Marine Science, William & Mary. https://doi.org/10.21220/V5BQ60

Odum, E.P., 1980. *The status of three ecosystem-level hypothesis regarding salt marsh estuaries: tidal subsidy, outwelling, and detritus-based food chains*. In: Kennedy, V.S. (Ed.), Estuarine

Perspectives, 485–495. New York: Academic Press. https://doi.org/10.1016/B978-0-12-404060-1.50045-9

Olson, M., M. Malonee, and M.E Ley. 2012. Guide to using Chesapeake Bay program water quality monitoring data, 159. U.S. Environmental Protection Agency, EPA 908-R-12–001.

Paerl, H.W., and J. Huisman. 2008. Blooms like it hot. *Science* 320 (5872): 57–28. https://doi.org/10.1126/science.1155398.

Parkhurst, D.L., and C.A.J. Appelo. 1999. User's guide to PHREEQC (Version 2): A computer program for speciation, batch-reaction, one-dimensional transport, and inverse geochemical calculations. Water-Resources Investigations Report, 99–4259. U.S. Geological Survey. https://doi.org/10.3133/wri994259

Peierls, B.L., N.S. Hall, and H.W. Paerl. 2012. Non-monotonic responses of phytoplankton biomass accumulation to hydrologic variability: a comparison of two coastal plain North Carolina estuaries. *Estuaries and Coasts* 35: 1376–1392. https://doi.org/10.1007/s12237-012-9547-2.

Plummer, L.N., and E. Busenberg. 1982. The solubilities of calcite, aragonite and vaterite in CO_2-H_2O solutions between 0 and 90˚C, and an evaluation of the aqueous model for the system $CaCO_3$-CO_2-H_2O. *Geochimica Et Cosmochimica Acta* 46: 1101–1040.

Qin, Q., and J. Shen. 2019. Pelagic contribution to gross primary production dynamics in shallow areas of York River, VA, U.S.A. *Limnology and Oceanography* 64: 1484–1499. https://doi.org/10.1002/Ino.11129.

Radtke, H., M. Lipka, D. Bunke, C. Morys, J. Woelfel, B. Cahill, M.E. Böttcher, S. Forster, T. Leipe, G. Rehder, and T. Neumann. 2019. Ecological ReGional Ocean Model with vertically resolved sediments (ERGOM SED 1.0): coupling benthic and pelagic biogeochemistry of the south-western Baltic Sea. *Geoscientific Model Development* 12: 275–320. https://doi.org/10.5194/gmd-12-275-2019.

Raymond, P.A., J.E. Bauer, and J.J. Cole. 2000. Atmospheric CO_2 evasion, dissolved inorganic carbon production, and net heterotrophy in the York River Estuary. *Limnology and Oceanography* 45: 1707–1717.

Raymond, P.A., and N.-H. Oh. 2009. Long term changes of chemical weathering products in rivers heavily impacted from acid mine drainage: Insights on the impact of coal mining on regional and global carbon and sulfur budgets. *Earth and Planetary Science Letters* 28 (1–2): 50–56. https://doi.org/10.1016/j.epsl.2009.04.006.

Raymond, P.A., J. Hartmann, R. Lauerwald, S. Sobek, C.P. McDonald, M. Hoover, D. Butman, R.G. Striegl, E. Mayorga, C. Humborg, P. Kortelainen, H. Durr, M. Meybeck, P. Ciais, and P. Guth. 2017. Global carbon dioxide emissions from inland waters. *Nature* 503: 355–359.

Raymond, P.A., and S.K. Hamilton. 2018. Anthropogenic influences on riverine fluxes of dissolved inorganic carbon to the oceans. *Limnolology and Oceanography Letters* 3 (3): 143–155. https://doi.org/10.1002/lol2.10069.

Reay, W.G. 2009. Water quality within the York River Estuary. *Journal of Coastal Research* 57: 23–39.

Reece, K.S. 2015. *Monitoring for HAB species in VA waters of Chesapeake Bay during 2015: Emerging HAB species in Chesapeake Bay* (annual report No. VIMSHAB617FY16). Richmond: Report submitted to the Virginia Department of Health.

Reece, K.S., E.M. Burreson, D.M. Gibson, S.S. Hildebrandt, and I. Fenwick. 2020. The Chesapeake Bay oyster: cobblestone to keystone. In: Cuker, B. (eds) *Diet for a Sustainable Ecosystem. Estuaries of the World*. Cham: Springer. https://doi.org/10.1007/978-3-030-45481-4_8

Regnier, P., L. Resplandy, R.G. Najjar, and P. Ciais. 2022. The land-to-ocean loops of the global carbon cycle. *Nature* 603: 401–410. https://doi.org/10.1038/s41586-021-04339-9.

Reithmaier, G.M.S., A. Cabral, A. Akhand, et al. 2023. Carbonate chemistry and carbon sequestration driven by inorganic carbon outwelling from mangroves and saltmarshes. *Nature Communications* 14: 8196. https://doi.org/10.1038/s41467-023-44037-w.

Ridlon, A.D., A. Marks, C.J. Zabin, D. Zacherl, B. Allen, J. Crooks, G. Fleener, E. Grosholz, B. Peabody, J. Toft, and K. Wasson. 2021. Conservation of Marine Foundation Species: learning from native oyster restoration from California to British Columbia. *Estuaries and Coasts* 44: 1723–1743. https://doi.org/10.1007/s12237-021-00920-7.

Roden, E.E., and J.H. Tuttle. 1993. Inorganic sulfur turnover in oligohaline estuarine sediments. *Biogeochemistry* 22: 81–105. https://doi.org/10.1007/BF00002706.

Salisbury, J., M. Green, C. Hunt, and J. Campbell. 2008. Coastal acidification by rivers: a threat to shellfish? *Eos, Transactions of the American Geophysical Union* 89 (50): 513–513. https://doi.org/10.1029/2008EO500001.

Santos, I.R., D.T. Maher, R. Larkin, J.R. Webb, and C.J. Sanders. 2019. Carbon outwelling and outgassing vs. burial in an estuarine tidal creek surrounded by mangrove and saltmarsh wetlands. *Limnology and Oceanography* 64: 996–1013. https://doi.org/10.1002/lno.11090.

Santos, I.R., D.J. Burdige, T.C. Jennerjahn, S. Bouillon, A. Cabral, O. Serrano, T. Wernberg, K. Filbee-Dexter, J.A. Guimond, and J.J. Tamborski. 2021. The renaissance of Odum's outwelling hypothesis in blue carbon science. *Estuarine, Coastal and Shelf Science* 255: 107361. https://doi.org/10.1016/j.ecss.2021.107361.

Savoie, A.M., A. Moody, M. Gilbert, K.S. Dillon, S.D. Howden, A.M. Shiller, and C.T. Hayes. 2022. Impact of local rivers on coastal acidification. *Limnology and Oceanography* 67: 2779–2795. https://doi.org/10.1002/lno.12237.

Scully, M.E., and C.T. Friedrichs. 2007a. The importance of tidal and lateral asymmetries in stratification to residual circulation in partially-mixed estuaries. *Journal of Physical Oceanography* 37: 1496–1511.

Scully, M.E., and C.T. Friedrichs. 2007b. Sediment pumping by tidal asymmetry in a partially-mixed estuary. *Journal of Geophysical Research* 112: C07028. https://doi.org/10.1029/2006JC003784.

Scully, M.E., A.P.M. Michel, D.P. Nicholson, and S. Traylor. 2022. Spatial and temporal variations in atmospheric gas flux from the Hudson River: the estuarine gas exchange maximum. *Limnology and Oceanography* 67: 1590–1603. https://doi.org/10.1002/lno.12154.

Shadwick, E.H., M.A.M. Friedrichs, R.G. Najjar, O.A. DeMeo, J.R. Friedman, F. Da, and W.G. Reay. 2019. High-frequency CO_2-system variability over the winter-to-spring transition in a coastal plain estuary. *Journal of Geophysical Research: Oceans* 124 (11): 7626–7642. https://doi.org/10.1029/2019JC015246.

Shchepetkin, A., and J. McWilliams. 2005. The regional ocean modeling system (ROMS): a split-explicit, free-surface, topography-following-coordinate ocean model. *Ocean Modeling* 9: 347–404. https://doi.org/10.1016/j.ocemod.2004.08.002.

Shen, J., and L. Haas. 2004. Calculating age and residence time in the tidal York River using three-dimensional model experiments. *Estuarine, Coastal and Shelf Science* 61: 449–461. https://doi.org/10.1016/j.ecss.2004.06.010.

Shen, C., J.M. Testa, M. Li, W.-J. Cai, G.G. Waldbusser, W. Ni, W.M. Kemp, J. Cornwell, B. Chen, J. Brodeur, and J. Su. 2019. Controls on carbonate system dynamics in a coastal plain estuary: a modeling study. *Journal of Geophysical Research: Biogeosciences* 124. https://doi.org/10.1029/2018JG004802.

Siedlecki, S.A., D.J. Pilcher, A.J. Hermann, K. Coyle, and J. Mathis. 2017. The importance of freshwater to spatial variability of aragonite saturation state in the Gulf of Alaska. *Journal of Geophysical Research: Oceans* 122 (11).

Sims, R.P., M. Bedington, U. Schuster, A.J. Watson, V. Kitidis, R. Torres, H.S. Findlay, J.R. Fishwick, I. Brown, and T.G. Bell. 2022. Tidal mixing of estuarine and coastal waters in the western English Channel is a control on spatial and temporal variability in seawater CO_2. *Biogeosciences* 19: 1657–1674. https://doi.org/10.5194/bg-19-1657-2022.

Stets, E.G., V.J. Kelly, and C.G. Crawford. 2014. Long-term trends in alkalinity in large rivers of the conterminous US in relation to acidification, agriculture, and hydrologic modification. *Science of the Total Environment* 488: 280–289. https://doi.org/10.1016/j.scitotenv.2014.04.054.

St. Laurent, K.A., V.J. Coles, and R.R. Hood. 2021. Climate Extremes and Variability Surrounding Chesapeake Bay: Past, Present, and Future. *Journal of the American Water Resources Association* 1– 29. https://doi.org/10.1111/1752-1688.12945

St-Laurent, P., M.A.M. Friedrichs, R.G. Najjar, E.H. Shadwick, H. Tian, and Y. Yao. 2020. Relative impacts of global changes and regional watershed changes on the inorganic carbon balance of the Chesapeake Bay. *Biogeosciences* 17 (14): 3779–3796. https://doi.org/10.5194/bg-17-3779-2020.

St-Laurent, P., and M.A.M. Friedrichs. 2024. On the sensitivity of coastal hypoxia to its external physical forcings. *Journal of Advances in Modeling Earth Systems* 16: e2023MS003845. https://doi.org/10.1029/2023MS003845.

Su, J., W.-J. Cai, J. Brodeur, B. Chen, et al. 2020. Chesapeake Bay acidification buffered by spatially decoupled carbonate mineral cycling. *Nature Geoscience* 13: 441–447. https://doi.org/10.1038/s41561-020-0584-3.

Tamborski, J.J., M. Eagle, B.L. Kurylyk, K.D. Kroeger, Z.A. Wang, P. Henderson, and M.A. Charette. 2021. Pore water exchange-driven inorganic carbon export from intertidal salt marshes. *Limnology and Oceanography* 66: 1774–1792. https://doi.org/10.1002/lno.11721.

Taylor, G.I. 1920. Tidal friction in the Irish Sea. *Philosophical Transactions of the Royal Society of London. Series A, Containing Papers of a Mathematical or Physical Character* 220, 1–33. http://www.jstor.org/stable/91129. Accessed 25 Jul 2022.

Thibault de Chanvalon, A., G.W. Luther, E.R. Estes, J. Necker, B.M. Tebo, J. Su, and W.-J. Cai. 2022. Influences of iron and manganese cycling on alkalinity in the redox stratified water column of Chesapeake Bay. *Biogeosciences* 20: 3053–3071. https://doi.org/10.5194/bg-20-3053-2023.

Turner, J.S., P. St-Laurent, M.A.M. Friedrichs, and C.T. Friedrichs. 2021. Effects of reduced shoreline erosion on Chesapeake Bay water quality. *Science of the Total Environment* 769: 145157. https://doi.org/10.1016/j.scitotenv.2021.145157.

Van Dam, B.R., J.R. Crosswell, and H.W. Paerl. 2018. Flood-driven CO_2 emissions from adjacent North Carolina estuaries during Hurricane Joaquin (2015). *Marine Chemistry* 207: 1–12. https://doi.org/10.1016/j.marchem.2018.10.001.

Van Dam, B.R., and H. Wang. 2019. Decadal-scale acidification trends in adjacent North Carolina estuaries: competing role of anthropogenic CO_2 and riverine alkalinity loads. *Frontier in Marine Science* 6: 136. https://doi.org/10.3389/fmars.2019.00136.

van Heuven, S., D. Pierrot, J.W.B. Rae, E. Lewis, and D.W. Wallace. 2011. *Matlab program developed for CO_2 system calculations* (Tech. Rep. ORNL/CDIAC-105b). Oak Ridge National Laboratory: Carbon Dioxide Information Analysis Center.

Vargas, C.A., L.A. Cuevas, B.R. Broitman, V.A. San Martin, N.A. Lagos, J.D. Gaitán-Espitia, and S. Dupont. 2022. Upper environmental pCO_2 drives sensitivity to ocean acidification in marine invertebrates. *Nature Climate Change* 12: 200–207. https://doi.org/10.1038/s41558-021-01269-2.

Waldbusser, G.G., E.P. Voigt, H. Bergschneider, M.A. Green, and R.I.E. Newell. 2011. Biocalcification in the Eastern Oyster (*Crassostrea virginica*) in relation to long-term trends in Chesapeake Bay pH. *Estuaries and Coasts* 34: 221–231. https://doi.org/10.1007/s12237-010-9307-0.

Wallace, R.B., H. Baumann, J.S. Grear, R.C. Aller, and C.J. Gobler. 2014. Coastal ocean acidification: the other eutrophication problem. *Estuarine, Coastal and Shelf Science* 148: 1–13.

Wang, Z.A., and W.-J. Cai. 2004. Carbon dioxide degassing and inorganic carbon export from a marsh-dominated estuary (the Duplin River): a marsh CO_2 pump. *Limnology and Oceanography* 49: 341–354. https://doi.org/10.4319/lo.2004.49.2.0341.

Wang, Z.A., K.D. Kroeger, N.K. Ganju, M.E. Gonneea, and S.N. Chu. 2016. Intertidal salt marshes as an important source of inorganic carbon to the coastal ocean. *Limnology and Oceanography* 61: 1916–1931. https://doi.org/10.1002/lno.10347.

Wang, Z.A., and Cai, W.-J. 2024. The inorganic carbon system across the land-to-ocean continuum. *In Reference Module in Earth Systems and Environmental Sciences*. Elsevier. https://doi.org/10.1016/B978-0-323-99762-1.00032-2.

Wanninkhof, R. 2014. Relationship between wind speed and gas exchange over the ocean revisited. *Limnology and Oceanography Methods* 12. https://doi.org/10.4319/lom.2014.12.351.

Warner, J.C., Z. Defne, K. Haas, and H.G. Arango. 2013. A wetting and drying scheme for ROMS. *Computers & Geosciences* 58: 54–61. https://doi.org/10.1016/j.cageo.2013.05.004.

Williams, M.R., T.R. Fisher, W.R. Boynton, C.F. Cerco, et al. 2006. An integrated modelling system for management of the Patuxent River estuary and basin, Maryland, USA. *International Journal of Remote Sensing* 27 (17): 3705–3726. https://doi.org/10.1080/01431160500500417.

Windham-Myers, L., W.-J. Cai, S.R. Alin, and A. Andersson et al. 2018. Chapter 15: Tidal wetlands and estuaries. In *Second state of the carbon cycle report (SOCCR2): A sustained assessment report*, eds. Cavallaro, N. et al., pp 596–648. US Global Change Research Program. https://carbon2018.globalchange.gov/chapter/15. Accessed 15 Feb 2022.

Wolf-Gladrow, D.A., R.E. Zeebe, C. Klaas, A. Körtzingera, and A.G. Dickson. 2007. Total alkalinity: the explicit conservative expression and its application to biogeochemical processes. *Marine Chemistry* 106 (1–2): 287–300. https://doi.org/10.1016/j.marchem.2007.01.006.

Yao, H., P.A. Montagna, M.S. Wetz, C.J. Staryk, and X. Hu. 2022. Subtropical estuarine carbon budget under various hydrologic extremes and implications on the lateral carbon exchange from tidal wetlands. *Water Research* 217: 118436. https://doi.org/10.1016/j.watres.2022.118436.

Yau, Y.Y., P. Xin, X. Chen, L. Zhan, M. Call, S.R. Conrad, C.J. Sanders, L. Li, J. Du, and I.R. Santos. 2022. Alkalinity export to the ocean is a major carbon sequestration mechanism in a macrotidal saltmarsh. *Limnology and Oceanography* 67 (S2). https://doi.org/10.1002/lno.12155.

Zhang, S., and N.J. Planavsky. 2019. Revisiting groundwater carbon fluxes to the ocean with implications for the carbon cycle. *Geology* 48. https://doi.org/10.1130/G46408.1.

Zhou, Y.Q., A.H. Sawyer, C.H. David, and J.S. Famiglietti. 2019. Fresh submarine groundwater discharge to the near-global coast. *Geophysical Research Letters* 46: 5855–5863. https://doi.org/10.1029/2019GL082749.